Neuromorphic Computation of Optic Flow Data

Final Report

Authors: Florent Valette, Franck Ruffier, Stéphane Viollet
Affiliation: Institut des sciences du mouvement, Marseille, France

ACT researchers: Tobias Seidl, Christos Ampatzis, Kevin de Groote

Date: July 2009

Contact:
Stephane.viollet@univmed.fr
Université de la Méditerranée, Aix-Marseille II

Advanced Concepts Team
Fax: +31(0)715658018
e-mail: act@esa.int

Available on the ACT website
http://www.esa.int/act

Ariadna ID: 08/6303b
Study Type: Standard
Contract Number: 21950

Contents

1 INTRODUCTION

Winged insects are able to navigate swiftly in unfamiliar environments by relying heavily on the optic flow (OF) [11] that is generated by their own motion [12]. For example, bees rely on OF to avoid obstacles [20, 22], to control their speed [15, 1] and height [2, 9], to cruise and land [24, 9, 23]. Recently, we developed the OCTAVE autopilot (see figure 1) based on a single ventral OF regulator for a miniature (100g) rotorcraft (see figure 2) [18]. The Octave autopilot was shown to enable this rotorcraft to carry out complex tasks such as ground avoidance and terrain following, to control risky maneuvers such as automatic take off and automatic landing (see figure 4) [17]. This OCTAVE autopilot was solely based on a single OF sensor 3[19]

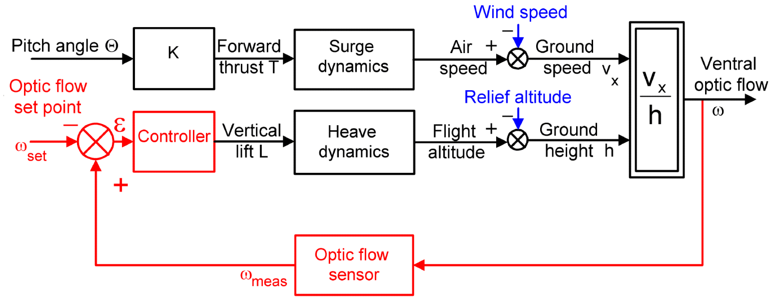

Figure 1: OCTAVE autopilot block diagram. Block diagram of the information flow giving the causal and dynamic relationships between sensory and motor variables. The upper (open loop) pathway describes how an increase in pitch angle Θ of the mean flight-force vector results in a proportional increase in forward thrust, and thus in ground speed V_x via the surge dynamics. The bottom (red) pathway shows how the ventral OF is measured (ω_{meas}) and compared with an OF set-point (ω_{set}). The error signal ($\epsilon = \omega_{meas} - \omega_{set}$) delivered by the comparator drives a controller adjusting the vertical lift L, and thus the ground height h via the heave dynamics, so as to maintain a constant OF ω (equal to ω_{set}), whatever the ground speed. The right part of this functional diagram depicts the system dynamics, defines the ventral OF as $\omega = V_x/h$, and shows the points at which two disturbances impinge on the system: the relief altitude subtracted from the flight altitude gives the ground height; and the wind speed subtracted from (by headwind) or added to (by tailwind) the airspeed gives the ground speed. Because ω is by definition an inverse function of the controlled variable h, the feedback loop is nonlinear (the non linearity is symbolized by the two nested rectangles). The controller includes proportional and derivative (PD) functions, which ensure closed-loop stability in the ground speed range of $0 - 3m.s^{-1}$.Adapted from[9].

Figure 2: Tethered miniature rotorcraft equipped with OCTAVE autopilot. The $100g$ miniature rotorcraft is tethered to the tip of a light panthographic arm (radius $1.9m$) that is free to rotate frictionlessly about a central pole. The miniature rotorcraft provides its own lift and is free to circle around with an unhindered, unlimited course over a flat surface (average track length per lap $12m$).[18]

Figure 3: An example of OF sensor based on the Franceschini's scheme. Adapted from [19]

The autopilot described here extends the OCTAVE autopilot principle to a Lunar lander. In this work, our goal was to make a lander landing safely i.e. by reaching the low gate (i.e., approximately 10 meters high with respect of the moon ground) at low speed (about 10m/s). The OF regulator adjusts the engine thrust so as to keep the OF equal to a set point. The outcome is that the lander ground speed and vertical speed will decrease during the landing phase. The autopilot enables the lander to perform safely lunar landing by measuring neither speed nor altitude. Our novel OF-based autopilot robustly regulates the ventral OF despite:

- the natural instability of the lander,
- the large parameter variations in altitude and speed due to the large working domain,
- the presence of many non-linearities in the Lander.

In section 2, we describe the dynamical model of the simulated lander. In section 3, the simulation set-up used to test the autopilot is described. Section 4 describe the autopilot in details. Section 5 shows the results of computer-simulated experiments carried out on the simulated lander which is able to land in various initial condition under various lighting condition and to react to a local absence of OF measurement during a few seconds. In the section 6, we compare Moon and Mars landing conditions, in section 7 we discuss about the effect of wind gust on Mars and then, in section 8 we talk about a way to estimate the Lander pitch using the Wide Field Integration.

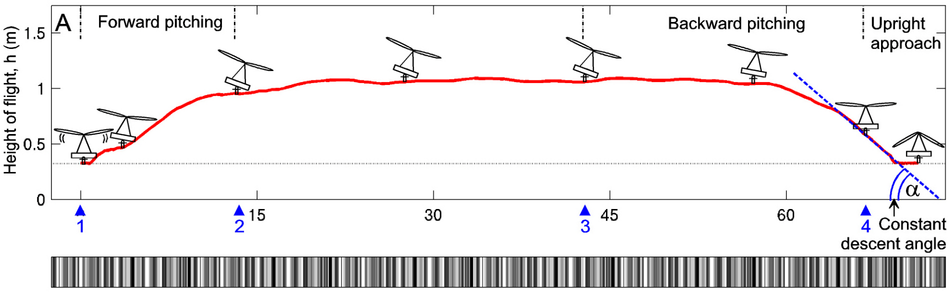

Figure 4: Trajectory of the miniature rotorcraft controlled by the OCTAVE autopilot. Vertical trajectory in the longitudinal plane. On the left, the operator simply pitched the miniature rotorcraft forward rampwise by an angle $\Delta\Theta = +10°$ (between arrowheads 1 and 2). The ensuing increase in ground speed (up to $3m.s^{-1}$) automatically triggered a proportional increase in ground height: the miniature rotorcraft climbed and flewlevel at a ground height of approximately 1 m, as dictated by the OF set-point ($\omega_{set} = 3rad.s^{-1}$, i.e., $172°.s^{-1}$). After flying 42 m, the miniature rotorcraft was simply pitched backward rampwise by an opposite angle $\Delta\Theta = -10°$ (between arrowheads 3 and 4), and the ensuing deceleration automatically initiated a proportional decrease in ground height until landing occurred. During the final approach, which started when the miniature rotorcraft had regained its completely upright position (arrowhead 4), the robot can be seen to have flown at a constant descent angle, as also observed in bees' landing performances [23]. Because the landing gear maintains the robot's eye 0.3 m above ground (dotted horizontal line), touchdown occurs shortly before the ground speed vx has reached zero, and the miniature rotorcraft ends its journey with a short ground run. Adapted from[9].

2 DYNAMICAL MODEL OF THE LANDER

Here, we described the dynamical model of the lander where :

- the main thruster command leads to altitude change along the heave axis

- the main thruster command leads through a pitch rotation to a change of the forward thrust along the surge axis. We consider that the attitudes (pitch, roll and yaw) are controlled by an other system. In addition, we do not consider any changes in yaw and roll: we rather considered that roll and yaw are maintained constant around an equilibrium value (adequate set point). In addition, we considered that the lander move in the $(\overrightarrow{x},\overrightarrow{z})$ plane. The simulated lander is not subject to any friction, wind or drag force due to an absence of atmosphere on the Moon.

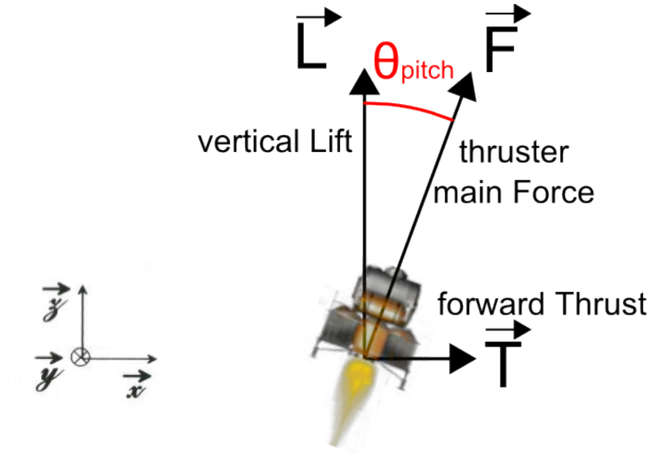

Figure 5: Resolution of the thruster mean Force vector $\overrightarrow{F}$ along the surge X-axis giving the forward Thrust $\overrightarrow{T}$ and along the heave Z-axis giving the vertical Lift $\overrightarrow{L}$. Pitching the thruster mean Force vector $\overrightarrow{F}$ by an angle θ_{pitch} generates a forward Thrust.

The lander is equipped with a twin-thruster engine: each thruster provides equally half of the lander mean Force vector $\overrightarrow{F}$. The pitch angle is supposed to be controlled by an adequate system. The lander decreases its forward speed by pitching backward at an angle θ_{pitch} (between -60 and $-30°$) with respect of the vertical (z axis). The thrusters main Force $\overrightarrow{F}$ can be resolved in forward Thrust T and vertical Lift L (see equation 1).

$$\begin{cases} T = F \cdot \sin\theta_{pitch} \\ \\ L = F \cdot \cos\theta_{pitch} \end{cases} \tag{1}$$

2.1 Thruster dynamics

The thruster model from thruster command $thruster_{cmd}$ to the thruster mean Force $\overrightarrow{F}$ is a first order system and its transfer function can be written as follows:

$$G_{thruster}(s) = \frac{F(s)}{Thruster_{cmd}(s)} = \frac{1/\tau_{thruster}}{1/\tau_{thruster} + s} = \frac{10}{10 + s} \tag{2}$$

The thruster can give only positive force and its maximum thrust is $100 \cdot m_{lander}$ $[N]$, so we can write: $0 \leq \frac{F}{m_{lander}} \leq 100$. Because the angle θ_{pitch} can not be considered as a small angle $(30° \leq |\theta_{pitch}| \leq 60°)$, each component of the thruster mean force can not be linearized as a function of the pitch angle θ_{pitch} along the surge ($\overrightarrow{x}$) and the heave ($\overrightarrow{z}$.) axes. According to the equations 1 and 2 we can write :

$$\begin{cases} m_{lander} \cdot (a_{thruster_z} + \tau_{thruster} \cdot \frac{da_{thruster_z}}{dt}) = L = F \cdot \cos\theta_{pitch} \\ \\ m_{lander} \cdot (a_{thruster_x} + \tau_{thruster} \cdot \frac{da_{thruster_x}}{dt}) = T = F \cdot \sin\theta_{pitch} \end{cases} \tag{3}$$

where $a_{thruster_z}$ and $a_{thruster_x}$ are respectively the acceleration given by the thruster along the X-axis, $\overrightarrow{x}$, and the Z-axis, $\overrightarrow{z}$, and m_{lander} the mass of the lander.

2.2 State-space model of the lander

The following system of equation define the dynamics of the lander at its center of gravity:

$$\begin{cases} L - m_{lander} \cdot g_{moon} = m_{lander} \cdot a_{lander_z} \\ \\ T = m_{lander} \cdot a_{lander_x} \end{cases} \tag{4}$$

where g_{moon} is the moon gravity constant, $g_{moon} = 1.63 m \cdot s^{-2}$, and $m_{lander} = 1 \cdot 10^3 kg$, the mass of the lander. By substituting the equations 2 and 3 in the equation 4 along the Z-axis $\overrightarrow{z}$, we can write :

$$\frac{F}{m_{lander}} \cdot \cos\theta_{pitch} - g_{moon} = \frac{d^2z}{dt^2} \tag{5}$$

So, the transfer function for heave dynamics $G_z(s)$ can be written as follows:

$$G_z(s) = \frac{Z(s)}{F(s)} = \frac{1}{s^2} \cdot \left[\left(\frac{1/\tau_{thruster}}{1/\tau_{thruster} + s} \cdot \cos\theta_{pitch}\right) - g_{moon}\right] \tag{6}$$

Along the X-axis $\overrightarrow{x}$, we can write :

$$\frac{F}{m_{lander}} \cdot \sin\theta_{pitch} = \frac{d^2x}{dt^2} \tag{7}$$

So, the transfer function for the surge dynamics $G_x(s)$ can be written as follows :

$$G_x(s) = \frac{X(s)}{F(s)} = \frac{1}{s^2} \cdot \left(\frac{1/\tau_{thruster}}{1/\tau_{thruster} + s} \cdot \sin\theta_{pitch}\right) \tag{8}$$

Because of the double integral term in the transfer function,we decided to write the lander's model with the state-space approach. State-space representation characterizes a system by a multivariable equation between the state X, the derived state $\dot{X}$, the input of the system u and the measured output y that we want to regulate:

$$\begin{cases} \dot{X} = A \cdot X + B \cdot u \\ \\ y = C \cdot X + D \cdot u \end{cases} \tag{9}$$

For the lander model, we choose the following state vector $X = \begin{bmatrix} h \\ V_z \\ a_{thruster_z} \end{bmatrix}$ and the following input $u = \left[\frac{L}{m_{lander}}\right]$. According to the equations 3 and 4, we can write:

$$\begin{cases} \dot{a}_{thruster_z} = 10 \cdot \left[\frac{L}{m_{lander}} - a_{thruster_z}\right] \\ \\ \dot{V}_z = a_{thruster_z} - g_{moon} \\ \\ \dot{h} = V_z \end{cases} \tag{10}$$

We can deduce from the equations 10 , the matrix A_p, B_p and a disturbance element g :

$$\begin{cases} \dot{X} = A_p \cdot X + B_p \cdot u - g \\ \begin{bmatrix} \dot{h} \\ \dot{V}_z \\ \dot{a}_{thruster_z} \end{bmatrix} = \begin{bmatrix} 0 & 1 & 0 \\ 0 & 0 & 1 \\ 0 & 0 & -10 \end{bmatrix} \cdot \begin{bmatrix} h \\ V_z \\ a_{thruster_z} \end{bmatrix} + \begin{bmatrix} 0 \\ 0 \\ 10 \end{bmatrix} \cdot \left[\frac{L}{m}\right] - \begin{bmatrix} 0 \\ g_{moon} \\ 0 \end{bmatrix} \end{cases} \tag{11}$$

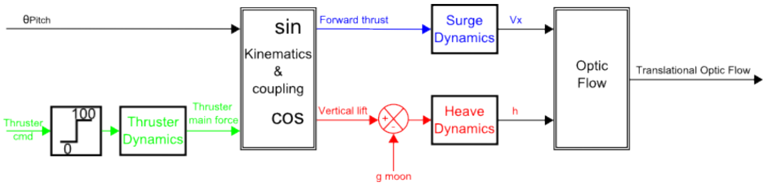

Figure 6: Kinematic and dynamical modeling of the Lander

2.3 Lander non-linearities and natural instability

The Lander system is quite delicate to control and to stabilize because of the amount of non-linearities and its natural instability:

- Thruster main force saturates in the range between 0 and $10^5 N$,
- Coupling between vertical lift and forward thrust by the Lander pitch,
- The permanent disturbance of the moon gravity,
- The heave control that acts upon the inverse of the regulated output (the optic flow),
- The instabilities due to a double integration and a first order low-pass filter between thruster main force and altitude changes,

3 SIMULATION SETUP

3.1 Simulated lunar surface

The simulated visual environment consists of lunar surface images generated by PANGU (Planetary and Asteroid Natural scene Generator Utility) [14] with respect to the altitude, the position of the lander and the maximum elevation of the sun. The images generated by PANGU are in 256 gray-scale levels. The image resolution is 256 × 256 pixels and one square pixel corresponds to 0.1° × 0.1° in the field of view.

3.2 Optic Flow generated by the motion of the lander

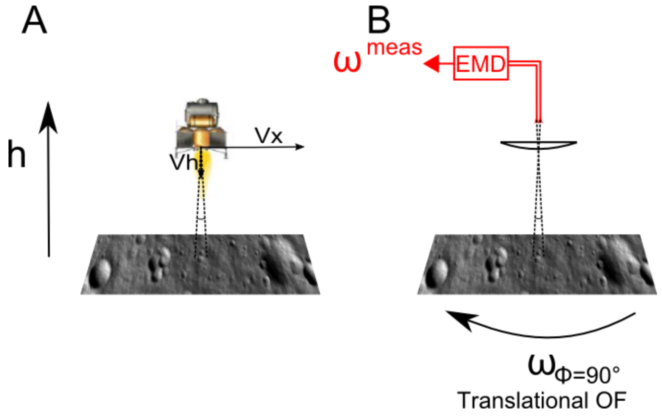

Figure 7: Generated and measured Optic flow.(A) The ventral OF perceived by the Lander flying at ground speedV_x and ground height h is the angular speed $\omega_{\Phi=90^\circ}$ at which a point in the moon surface directly below seems to move in the opposite direction. The moon ground shown here is an image sample from PANGU. (B) A simulated minimalistic "OF sensor" used on-board the Lander comprises a micro lens and two photo-receptors driving as fly-inspired elementary motion detector (EMD). The output $\omega_{meas_{\Phi=90^\circ}}$ from the OF sensor will serve as a feedback signal in the control scheme in figure 11

The lander flies at a ground speed vector $\overrightarrow{V_x}$ and a vertical speed vector $\overrightarrow{V_z}$ over the lunar surface images generated by PANGU. The simulated lander is assumed to stabilize its gaze by compensating for any rotations around the roll and pitch axes. Since any rotation is compensated, the OF sensor will receive a purely translational OF, which is the angular velocity of lunar surface projected onto ventral OF sensor. The translational OF can be defined simply by the ground speed / ground height ratio according to the equation 12.

$$\omega_{\Phi=90^\circ} = \frac{V_x}{h} \tag{12}$$

where V_x is the forward speed of the lander and h is the ground height of the lander (see figure 7) .

3.3 OF sensor on-board the simulated lander

The OF sensor is mounted vertically downward with respect to the simulated lander symmetry axis. The OF sensor is composed of only two photo-receptors (two pixel) driving an Elementary Motion Detector (EMD). The visual axes of the two photoreceptors are separated by an inter-receptor angle $\Delta\phi = 2^\circ$. Each photoreceptor angular sensitivity is a 2D Gaussian function with an acceptance angle (angular width at half height) $\Delta\rho = 2^\circ$ (see figure 8). According to [21], we choose the same angle for the inter receptor angle and the acceptance angle. Each photoreceptor covers a field of view of 5° × 5°. The photoreceptor output is computed at

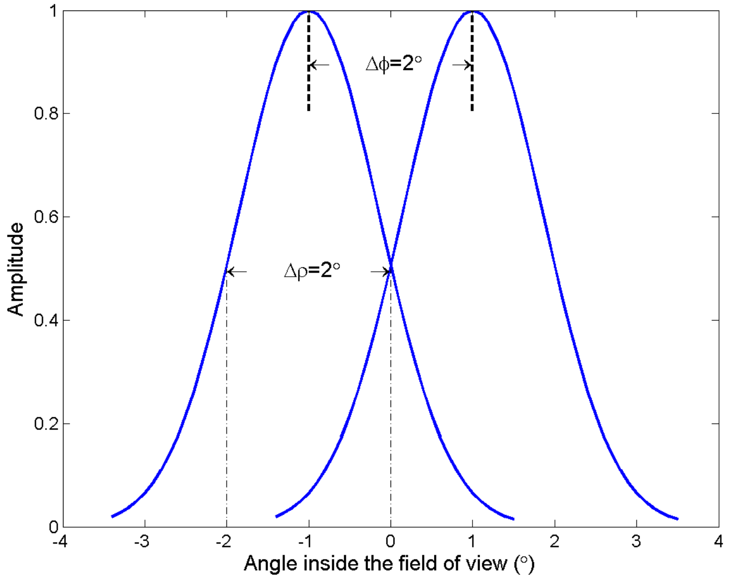

Figure 8: Gaussian sensitivity and inter-receptor angle between photo-receptors

each time step (1msec) by convolving the lunar surface image from PANGU with a 2D Gaussian filter that mimics the photoreceptor Gaussian sensitivity.

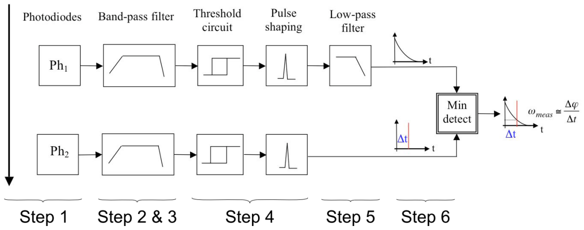

Figure 9: Fanceschini et Al's elementary motion detector scheme [10]

In order to measure the OF on the moon, we have to calibrate the time constant τ_{DEM} of the decreasing exponential of the EMD to make the OF sensor measuring the OF range generated by the Lander. According to the range of speed and altitude of the lander during the landing, the range of OF is between 10 and $30^{\circ} \cdot s^{-1}$. According to the inter-receptor angle, we set the time constant of the final low pass filter (see figure 9) to $\tau_{EMD} = 0.1s$. With these parameters, the characteristic of the OF sensor is given by the figure 10. The OF sensor responds as a monotonic function of the angular velocity within an OF range from $4.5^{\circ} \cdot s^{-1}$ to $45^{\circ} \cdot s^{-1}$.

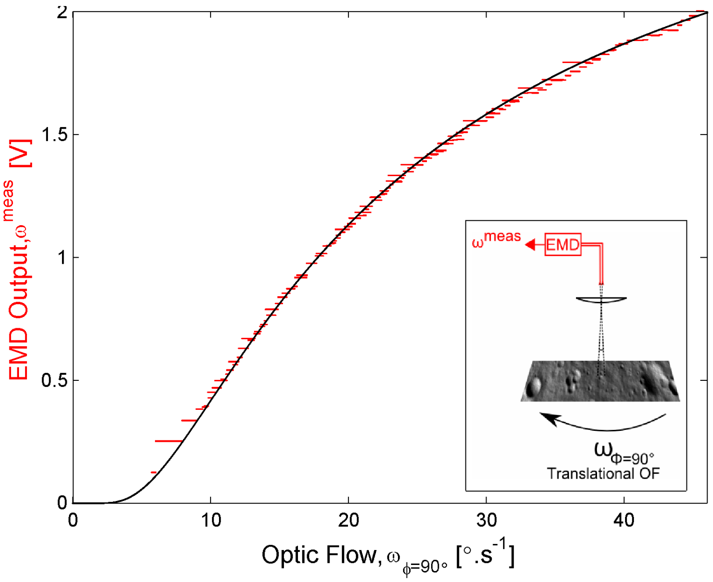

Figure 10: EMD Input/Output characteristics stimulated by Moon image velocities generated by PANGU. Analog EMD output (in Volts) (red lines) versus angular velocity. This figure shows the EMD response to several motion stimuli at various angular speed. These data were collected using the images producing by PANGU. The EMD circuit's response (red plot) is monotonic with respect of the angular velocity. In order to obtain this input/output characteristics on moon, we applied to the lander a ground speed variation in ramp at different altitude.

The EMD principle [7, 3, 4] is inspired by the results of experiments on the fly that combined electrophysiological recordings and light micro stimulation of the retina [6, 8]. The EMD principle consists in the following six steps (see figure 9):

Step1: Spatial low-pass filtering is achieved here by placing the photo-receptors between the focal plane and the lens (defocusing) . Unlike insects in which spatial low-pass filtering automatically results from diffraction, the cut-off spatial frequency depends on the amount of defocusing.

Step2: High-pass temporal filtering (cut-off frequency: $20Hz$) of the signals in each channel to cancel the dc component and discriminate between ON and OFF transitions.

Step3: Low-pass temporal filtering (cut-off frequency: $30Hz$) to reduce noise and interference.

Step4: Thresholding and pulse generation are performed on the signals in each channel for contrast detection.

Step5: Long time decreasing exponential (time constant τ_{EMD}, several milliseconds) generation on channel 1, determining the range of the delay Δt considered, and thus the range of measures of the EMD.

Step6: Sampling of the exponential of the channel 1 by the pulse of the channel 2 in order to approximate the Optic Flow. The output of the EMD can be written as follows :

$$\omega^{meas} = k \cdot e^{\frac{-\Delta\phi}{\omega \cdot \tau_{EMD}}} \tag{13}$$

4 THE AUTOPILOT

In this section, we will treat about the design of the autopilot. The autopilot relies on a single OF measurement (ventral OF) and it consists of a visuomotor feedback loop which is driven the thruster main force. The aim of the autopilot is to keep the OF measured equal to the setting value. The loop operates on the heave and the surge axis due to the coupling between the vertical lift and the forward thrust. The pitch angle θ_{pitch} is controlled by an external system. The lander will pitch backward from $-60°$ to $-30°$ during the landing. The control loop consists in a precompensation gain, a non linear states observer and a states feedback gain. The non linear states observer estimates the state of the lander by using the measured output of the system, i.e., ventral OF ω^{meas} and the lander acceleration a_{lander_z} (see figure 11).

4.1 Control law based on full State feedback

In order to keep the ventral OF of the simulated lander at the ω_{set} value, the product between the state feedback gain L_{sf} and the estimated states $\widehat{X}$ (see equation 18) is compared to the input of the autopilot. Before computing the control law, which is defined by the gain L_{sf}, we must check if the system is controllable by computing the rank of its controllability matrix Cmd. The system is controllable if and only if the rank of the matrix equals the number of states. The Cmd matrix is given by the following equation:

$$Cmd = \begin{bmatrix} B_p & (A_p \cdot B_p) & (A_p^2 \cdot B_p) \end{bmatrix} = \begin{bmatrix} 0 & 0 & 10 \\ 0 & 10 & -100 \\ 10 & -100 & 1000 \end{bmatrix} \tag{14}$$

The rank the Cmd matrix equals the number of states (i.e., three), so we can compute the state feedback gain with respect of the classical lqr method [5] where:

$$\int_0^{+\infty} \left(\left(X^T \cdot Q_c \cdot X + u^T \cdot R_c \cdot u \right) \cdot dt \right) \tag{15}$$

is the criterion to minimize using the following matrix: $A_{sf} = A_p$, $B_{sf} = B_p$ and $C_{sf} = \begin{bmatrix} K_{lin} & 0 & 0 \end{bmatrix}$ and the pondering matrix $Q_c = \begin{bmatrix} 7.8 \cdot 10^{-4} & 0 & 0 \\ 0 & 0 & 0 \\ 0 & 0 & 0 \end{bmatrix}$ and $R_c = [1]$. To compute the C_{sf} matrix, we choose to linearize the OF expression near a set point, here the set point is $h_{lin} = 200m$, $V_{x_{lin}} = 50m \cdot s^{-1}$ and $\omega = 14.3° \cdot s^{-1}$. The non linear OF definition in $\frac{1}{h}$ is approximated by its tangent's slope and thus by the following gain:

$$K_{lin} = V_{x_{lin}} \cdot \frac{d}{dh} \left(\frac{1}{h} \right)_{h=h_{lin}} = \frac{-V_{x_{lin}}}{h_{lin}^2} \tag{16}$$

4.2 Precompensation gain

To have a output equals to the set point ω_{set} [5], we compute a precompensation gain kr in order to have unitary static gain. the expression of the precompensation gain is given by:

$$kr = \frac{1}{C_{sf} \cdot (-A_{sf} + B_{sf} \cdot L_{sf})^{-1} \cdot B_{sf}} \tag{17}$$

4.3 Non linear states observer

A state observer is defined by the following equation :

$$\begin{cases} \dot{\widehat{X}} = A_o \cdot \widehat{X} + B_o \cdot u + K_o \cdot (y - \widehat{y}) \\ \\ \widehat{y} = C_o \cdot \widehat{X} + D_o \cdot u \end{cases} \tag{18}$$

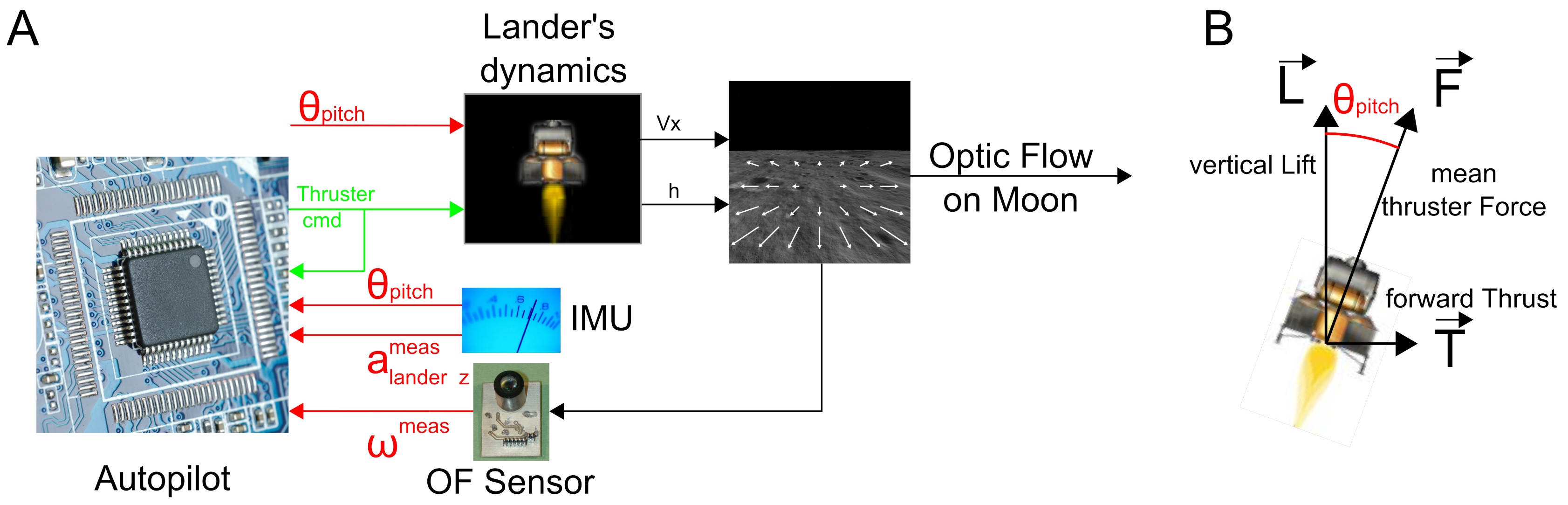

Figure 11: Overall feedback loop to control the ventral OF. (A) Information flow outlining the causal and dynamic relationship between sensory and thruster variable. The upper (open loop) pathway describes the decrease in pitch angle θ_{pitch} of the thrusters main force (see B) and the resulting coupled decrease in forward thrust and increase in vertical lift. In the bottom pathway ventral OF and vertical acceleration are used to adjust the Thruster main force, thus the ground height h via the heave dynamics, so as to maintain OF ω^{meas} constant.

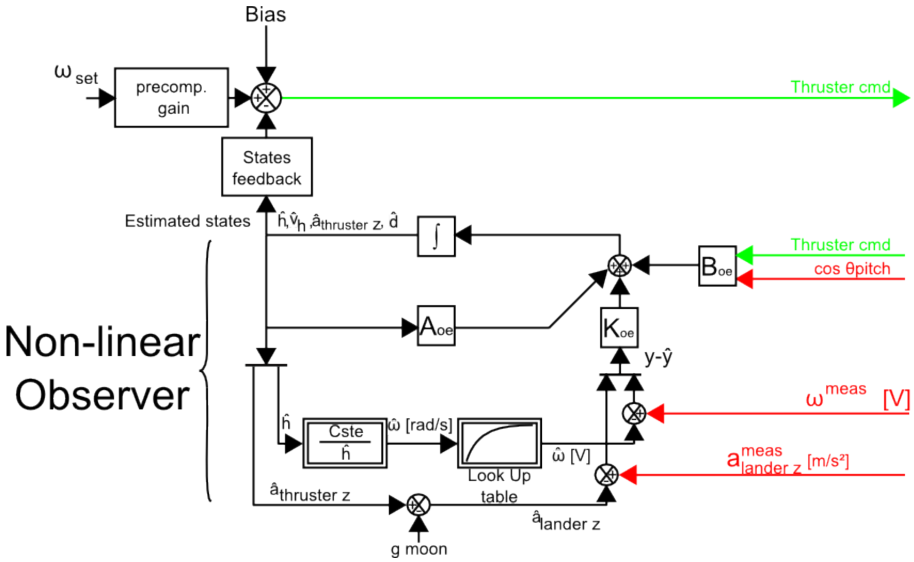

Figure 12: Block diagram of the non-linear observer that provides the estimated states to the feedback control scheme. The observer is nonlinear because ω is by definition an inverse function of the controlled variable h. The estimation of the OF in $rad \cdot s^{-1}$ is computed by the ratio between a constant (ground speed at a working point) and the estimated height of the lander $\widehat{h}$. The optic flow is then obtained via a look-up table. The measured acceleration of the lander $a_{lander_z}^{meas}$ serves for an improved estimation of the states. The estimated acceleration $\widehat{a}_{lander_z}$ results from subtracting the approximated gravity on the Moon g_{moon}, from the estimated acceleration produced by the thruster $\widehat{a}_{thruster_z}$.

where $A_o = A_{sf}$, $B_o = B_{sf}$, $C_o = \begin{bmatrix} & C_{sf} & \\ 0 & 0 & 1 \end{bmatrix}$, $D_o = [0]$ and K_o (Observer gain) are computed by applying the lqr method as well. The $\widehat{X}$ and the $\hat{\dot{X}}$ are respectively the estimated state and the estimated derivated state. $\widehat{y}$ is the estimated output of the system.

The C_o matrix has a additional term compare to the C_{sf} matrix because the lander acceleration a_{lander_z} is measured in order to help the observer to have a better estimation of the states but the acceleration is not controlled by the loop. In order to build a states observer, we must check if the system is observable. A system is observable if and only if the rank of its matrix equals the number of states. The observability matrix of the simulated lander is given by the following equation:

$$O = \begin{bmatrix} C_o \\ C_o \cdot A_o \\ C_o \cdot A_o^2 \end{bmatrix} = \begin{bmatrix} K_{lin} & 0 & 0 \\ 0 & 0 & 1 \\ 0 & K_{lin} & 0 \\ 0 & 0 & -10 \\ 0 & 0 & K_{lin} \\ 0 & 0 & 100 \end{bmatrix} \tag{19}$$

The rank of the observability matrix is equal to the number of states, so we can observe the states of the simulated lander with an observer. In order to implement an integral control [5], we modeled a constant prediction ($\dot{d} = 0$) and thus we defined an augmented (integral) state vector $\widehat{X_e} = \begin{bmatrix} \widehat{X} \\ d \end{bmatrix}$. Because of this new state, the new state matrix can be written as follows:

$$\left\{\begin{array}{l} A_{oe} = \begin{bmatrix} & A_o & & B_o \\ 0 & 0 & 0 & 0 \end{bmatrix} \\ \\ B_{oe} = \begin{bmatrix} B_o \\ 0 \end{bmatrix} \\ \\ C_{oe} = \begin{bmatrix} C_o & \begin{matrix} 0 \\ 0 \end{matrix} \end{bmatrix} \end{array}\right. \tag{20}$$

and the new states feedback gain L_{sfe} is equal to:

$$L_{sfe} = \begin{bmatrix} L_{sf} & 1 \end{bmatrix} \tag{21}$$

The observer gain for the augmented states is compute with the same method but using the new states matrix (A_{oe} and C_{oe}) [5] thanks to the fact that the system still observable. Because of the range of ground speed during the landing, we can not use the C_{oe} matrix to compute the estimated OF ($\widehat{\omega}^{meas}$) and the estimated acceleration of the lander ($\widehat{a}_{lander_z}$). So the observer is non linear, to have an estimation of the OF in $rad \cdot s^{-1}$, the ratio between a constant (ground speed at a working point $V_{x_{lin}}$) and the estimated height of the lander $\widehat{h}$ is computed. Then, the estimated OF ($\widehat{\omega}^{meas}$) in Volt is obtained via a look-up table. The estimation of the acceleration of the lander ($\widehat{a}_{lander_z}$) is obtained by subtracting the moon gravity acceleration (g_{moon}) to the estimated acceleration given by the thruster ($\widehat{a}_{lander_z}$) (see figure12) .

5 SIMULATION RESULTS

5.1 Automatic landing

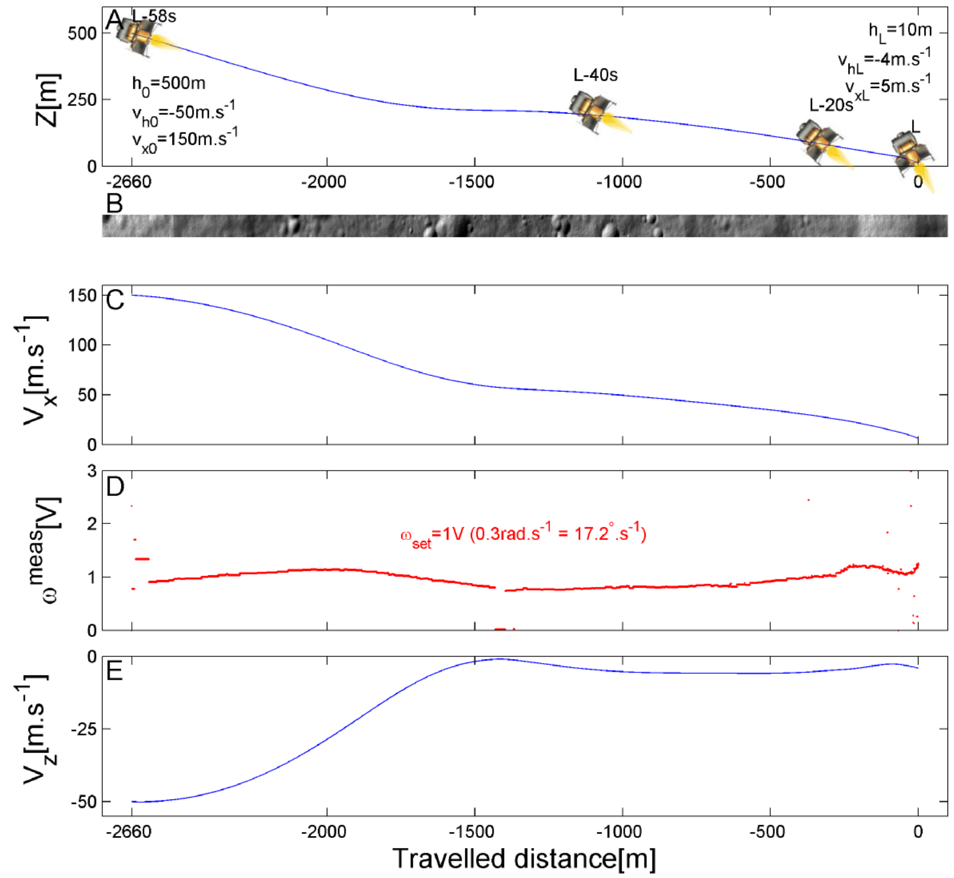

Figure 13: Automated landing using a bio-mimetic OF sensor and a bio-inspired strategy. The automatic landing lasts $58.4s$, starting from an initial height of $500m$, with an initial ground speed of $150m \cdot s^{-1}$ and an initial vertical speed of $50m \cdot s^{-1}$. (A) Vertical trajectory in the longitudinal plane. At $L - 58.4s$ ($58.4s$ before landing), the pitch angle θ_{pitch} equals $-60°$ and decrease to $-30°$ at $L - 10s$. The ensuing decrease of ground speed ($150m \cdot s^{-1}$ to less than $10m \cdot s^{-1}$ at $L - 10s$) automatically decreases the ground height and the vertical speed in order to keep the measured OF close to the set-point. (B) Moon surface seen as presented to the simulated lander during the entire landing phase. (C) Ground speed V_x was monitored throughout the landing. (D) Output ω^{meas} of the OF sensor was monitored during the landing and shows that the OF remains relatively constant during the landing, $\omega_{set} = 1V(0.3rad \cdot s^{-1} = 17.2° \cdot s^{-1})$. (E) Vertical speed V_h was monitored during the landing.

In figure 13, the lander reaches automatically the low gate (approximately 10 meters high) at low speed. The Lunar surface seen by the lander is gray-scale images generated by PANGU. The simulated lander starts its automatic landing at an initial altitude $Z_o = 500m$, an initial ground speed $V_{x_0} = 150m \cdot s^{-1}$ and an initial vertical speed $V_{h_0} = -50m \cdot s^{-1}$. Figure 13A shows the trajectory in the vertical plane (x,z) and the position of the lander when it reaches the low gate and every $20 seconds$ before. During the landing, the lunar surface seen by the lander is shown in Figure 13B. The initial pitch angle θ_{pitch} decreases exponentially from $-60deg$ to $-30deg$ (see figure 14), by consequence reducing exponentially its forward speed (see figure13C). Its vertical speed then reduces also exponentially (see figure13F) because its integral -h- is reduced exponentially to keep the ratio v_x/h -the OF measured ω_{meas}- constant near the set point value ω_{set} (see figure13D).

The theoretical OF ω_{th} is plotted during the automated landing (see figure13E) and we can

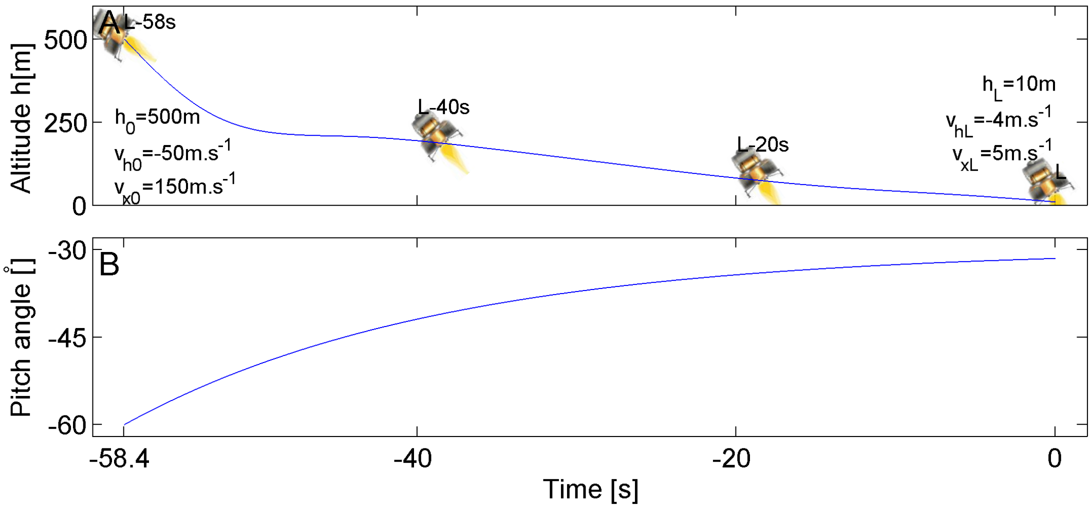

Figure 14: Pitch variation during the landing phase with respect of the time. (A) Vertical trajectory in the longitudinal plane. At $L - 58.4s$ (58.4s before landing), the pitch angle θ_{pitch} equals $-60°$ and decrease to $-30°$ at$L - 10s$. The ensuing decrease of ground speed ($150m \cdot s^{-1}$ to less than $10m \cdot s^{-1}$ at $L - 10s$) automatically decrease the ground height and the vertical speed in order to keep constant the OF. (B) Pitch angle θ_{pitch} variation during the landing duration.

see that the theoretical OF ω_{th} and the measured OF ω_{meas} are quite similar. We noticed an exception that occurs while the altitude of the lander is low: in fact, we can't compute accurately the theoretical OF because the height over the moon is not accurately known. The true height over the moon is quite different compared to the altitude given as parameter for the PANGU image generation because of the terrain of the moon (i.e. for an altitude given as parameter the ground height is different). The landing duration is $58.4s$ and the lander reach the low gate with a final ground speed $V_{x_L} = 5m \cdot s^{-1}$ and a final vertical speed $V_{h_L} = -4m \cdot s^{-1}$ and the distance traveled by the lander during the landing is $2660meters$.

5.2 Effect of various pitch law

The pitch law determines the plant's pitching reaction on the EMDs output signal. It has significant influence on the spacecraft's behavior. We investigate the landing performance according to different laws controlling pitch in open loop. The tested pitch law are defined, as follows:

- Exponential decreasing law with different time constants ($\tau = 15s$, $\tau = 20s$ and $\tau = 25s$) from $-60°$ to $-30°$ (see figure 16),

- Linear decreasing law from $-60°$ with different slope (1, 0.5, 0.25, 0.125 $° \cdot s^{-1}$)(see figure 17),

- Constant pitch of $-60°$(see figure 17).

The laws were applied to the setup described above and automatic landing had to be performed on the following initial conditions: $h_0 = 500m$, $v_{h0} = 50m.s^{-1}$, $v_{h0} = 150m.s^{-1}$. In any case, the upper thruster saturation of $100.m_{lander}$ was never reached. To assess the quality of the landing test, we compared in Tab. 1 the following final parameters of the Lander:

- the landing duration,

- the final vertical speed at the low gate,

- the final horizontal speed at the low gate,

- a fuel-consumption criterion, which is the integral of the thrust (see equation 22),

- the final pitch of each trial.

$$Consumption = \int_0^{T_{landing}} Thruster_{cmd}(t) \cdot m_{lander} dt \tag{22}$$

A slow linear decrease of the pitch (0.25 or 0.125 $^\circ \cdot s^{-1}$) allows a faster landing and an accurate decrease in vertical and horizontal speeds that reach a few meter per second at the low gate.

Pitch Law	**Exponential**			**Linear**				**Const**
Parameter	$\tau = 25s$	$\tau = 20s$	$\tau = 15s$	$1deg \cdot s^{-1}$	$0.5deg \cdot s^{-1}$	$0.25deg \cdot s^{-1}$	$0.125deg \cdot s^{-1}$	—
Landing duration $[s]$	55.2	**58.4**	74.7	63.3	38.8	30.3	25.4	21.
Final V_{x_l} $[m.s^{-1}]$	4.07	**7.25**	4.8	5.91	4.01	2.12	3.98	10.8
Final V_{h_l} $[m.s^{-1}]$	-3.72	**-3.69**	-6,43	-5.27	-4.52	-3.75	-2.69	-4.6
Consumption$/m_{lander}$	201.4	**200**	222.7	210	182.2	176	170.9	160
Pitch at touch down $[^\circ]$	-33.3	**-31.6**	-30.2	-30	-40.8	-52.4	-56.4	-60
Comment	Typical	**Typical**	Overshoot	Slow	Nice	Nice	Very short	Too f

Table 1: Comparison between different landing with respect to the consumption and the final pitch

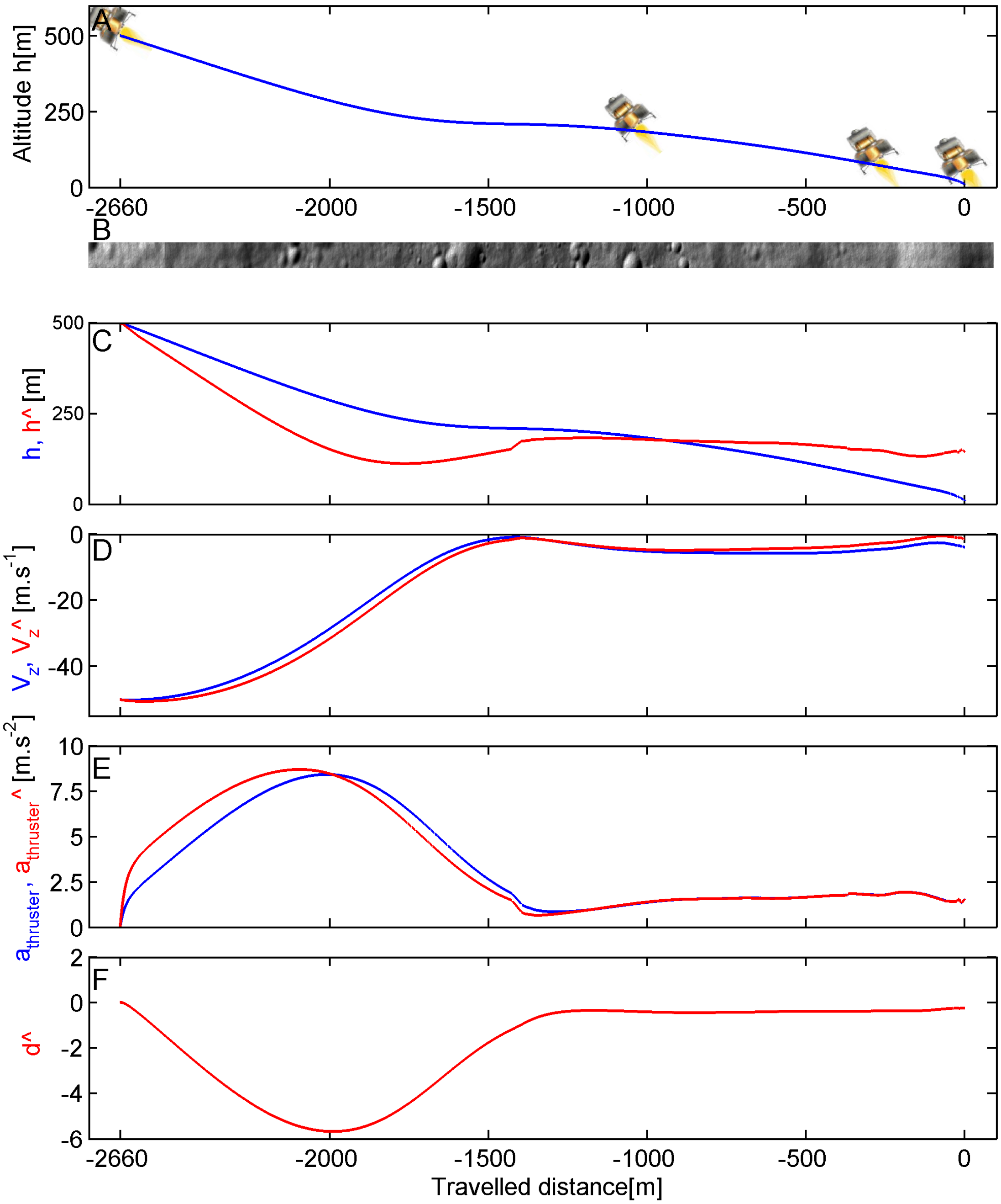

Figure 15: Comparison between "true" states (blue line) and estimated states (red line). (A) Vertical trajectory in the longitudinal plane. At $L - 58.4s$ (58.4s before landing), the pitch angle θ_{pitch} equals $-60°$ and decrease to $-30°$ at $L - 10s$. The ensuing decrease of ground speed ($150 m \cdot s^{-1}$ to less than $10 m \cdot s^{-1}$ at $L - 10s$) automatically decrease the ground height and the vertical speed in order to keep constant the OF. (B) Moon surface seen by the lander during the landing duration. (C) Comparison between "true" height (blue plot) and the estimated height (red plot). The estimated height is nearly constant in the second half of the landing phase because we use a non linear observer who estimates the OF measured $\widehat{\omega}^{meas}$ defined by the ration between a constant and the estimated height. (D)Comparison between the "true" vertical speed (blue plot) and the estimated vertical speed (red plot), the estimation is quite good because we measure the acceleration of the lander which is helping the observer to estimate the state. (E) Comparison between the acceleration given by the thruster $a_{thruster_z}$ (blue plot) and the estimated one $\widehat{a}_{thruster_z}$ (red plot). (F) Extended state during the landing, in order to have integral regulation.

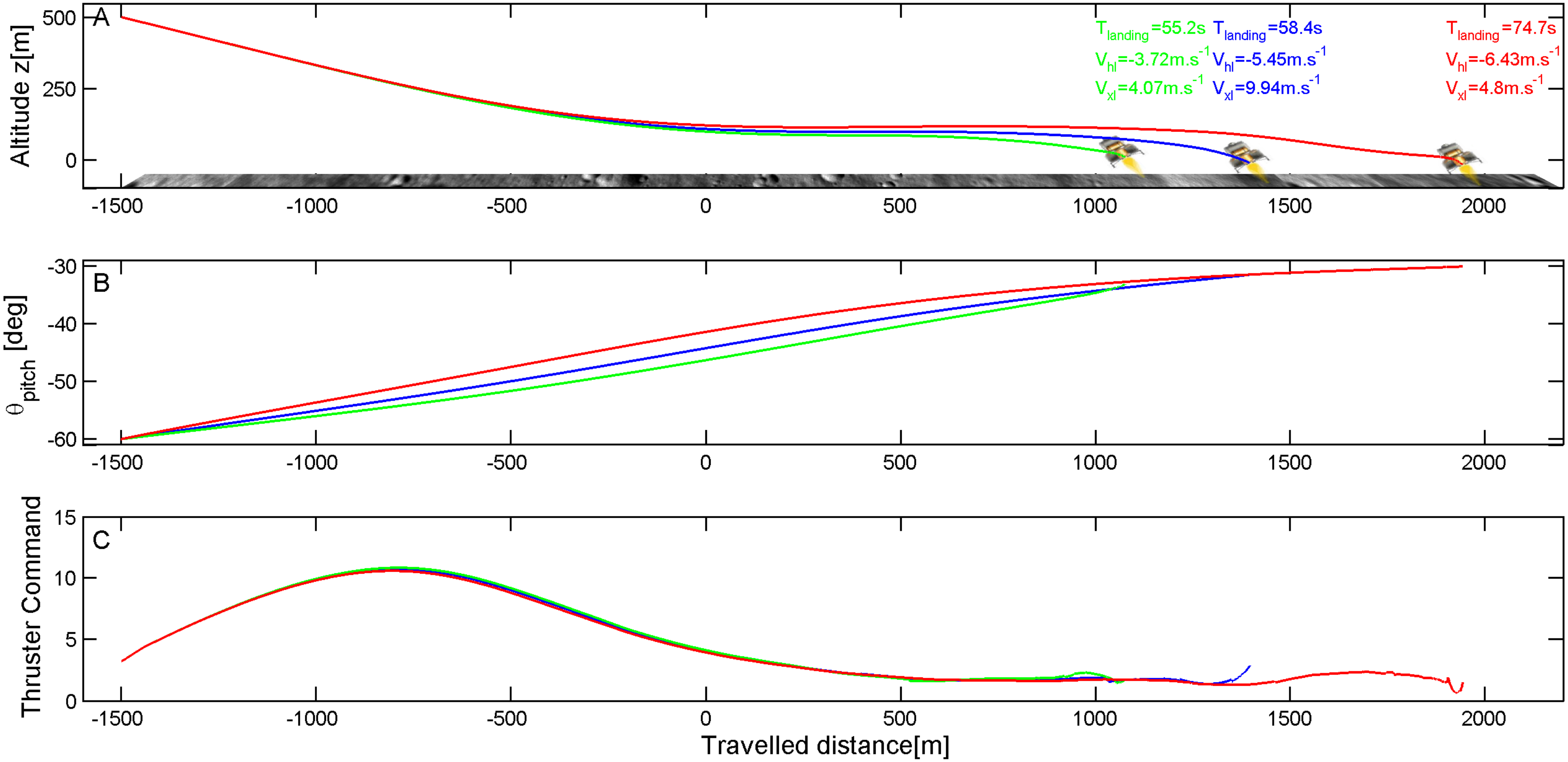

Figure 16: Automatic landing using an exponential pitch decay law with different time constant. (A) We show automatic landing trajectories using different time constant for its pitch decaying law ($\tau = 25s$ in green, $\tau = 20s$ in blue and $\tau = 15s$ in red) with an initial ground speed $V_{x0} = 150m \cdot s^{-1}$, an initial vertical speed $V_{z0} = -50m \cdot s^{-1}$ and an initial altitude $Z_0 = 500m \cdot s^{-1}$. The lander is plotted at the end of the trajectory to visualize its final pitch θ_{pitch}. In each case, the lander reached successfully the low gate (i.e. 10 meters high) with acceptable speeds. (B) Pitch angle θ_{pitch} of the lander during the landing. (C) Command applied to the thruster during the landing phase.

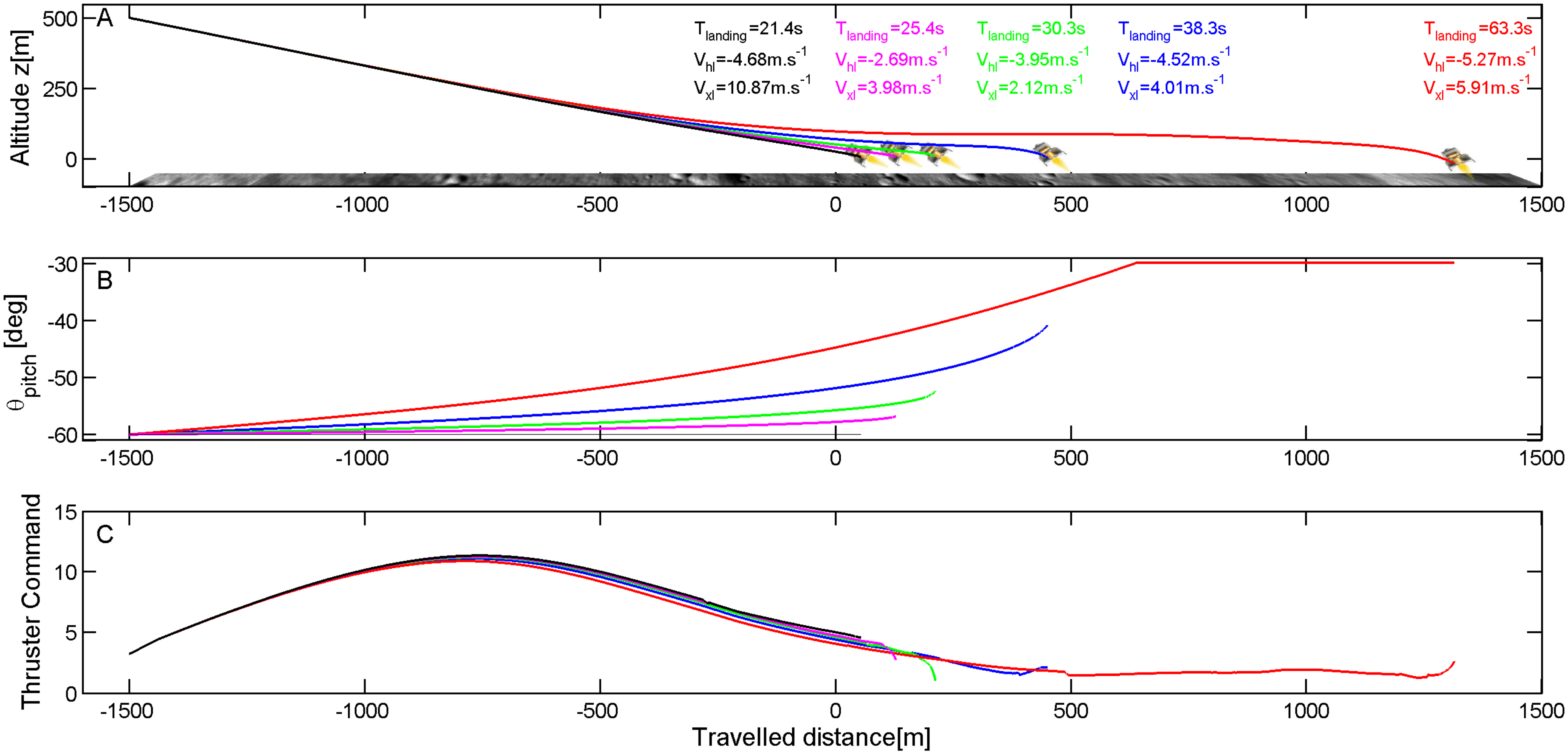

Figure 17: Automatic landing using a linear pitch decay law with different slope. (A) We show automatic landing trajectories of a lander using different slope for the linear pitch decaying law ($1deg \cdot s^{-1}$ in red, $0.5deg \cdot s^{-1}$ in blue, $0.25deg \cdot s^{-1}$ in green, $0.125deg \cdot s^{-1}$ in magenta and $0deg \cdot s^{-1}$ in black) with an initial ground speed $V_{x0} = 150m \cdot s^{-1}$, an initial vertical speed $V_{z0} = -50m \cdot s^{-1}$ and an initial altitude $Z_0 = 500m$. The lander reach successfully the low gate for a slope equals to 1, 0.5, 0.25, $0.125deg \cdot s^{-1}$ but the lander crashes for a constant pitch during the landing phase. The lander is plotted at the end of each trajectory to visualize its final pitch angle θ_{pitch}. (B) Pitch angle θ_{pitch} of the lander during the landing. (C) Command applied to the thruster during the landing phase.

5.3 Effect of various initial conditions

5.3.1 Different initial height

The figure 18 shows the influence of various initial altitude on the landing with an initial ground speed $V_{x0} = 150 m \cdot s^{-1}$and an initial vertical speed $V_{h0} = -50 m \cdot s^{-1}$. The figure shows the lander trajectory in the vertical plane (x,z) and the lander when it reaches the low gate and every 20 seconds before, for a starting altitude of $750m$, $500m$ and $250m$. As the pitch reduces the forward speed, the lander automatically adjusts the thrusters' main force to keep its ventral OF near the set point through the landing. With a starting altitude of $500m$ and $750m$ the lander reaches successfully the low gate with an acceptable ground speed and vertical speed. But in the case of a very low starting altitude (here $250m$), the ventral OF increase too fast and the autopilot can not stabilize the ventral OF and thus the lander reaches the low gate with a high ground speed $V_{x_l} = 77.4 m \cdot s^{-1}$ and a high vertical speed $V_{h_l} = -12.7 m \cdot s^{-1}$: the lander will probably crash. To summary, the earlier the optic flow regulation is used, the safer the landing phase.

5.3.2 Different initial ground speed

The figure 19 shows the influence of various initial ground speed on the landing with an initial altitude $Z_0 = 500m$ and an initial vertical speed $V_{h0} = -50 m \cdot s^{-1}$. The figure shows the lander trajectory in the vertical plane (x,z) and the lander when it reach the low gate and every 20 *seconds* before, for an initial ground speed of $200 m \cdot s^{-1}$, $150 m \cdot s^{-1}$ and $100 m \cdot s^{-1}$. As the pitch reduces the forward speed, the lander automatically adjusts the thruster main force in order to keep its ventral OF near the set point through the landing. The lander reaches successfully the low gate with an acceptable ground speed and vertical speed for each different initial ground speed (i.e. $200 m \cdot s^{-1}$, $150 m \cdot s^{-1}$ and $100 m \cdot s^{-1}$). Larger is the initial ground speed, farther is the distance traveled by the Lander before reaching the low gate (thus, increasing the time taken by the Lander to land on Moon).

5.3.3 Different initial vertical speed

The figure 20 shows the influence of various initial vertical speed on the landing with an initial altitude $Z_0 = 500m$ and an initial ground speed $V_{x0} = 150 m \cdot s^{-1}$. The figure shows the lander trajectory in the vertical plane (x,z) and the lander when it reaches the low gate and every 20 *seconds* before, for an initial vertical speed of $-100 m \cdot s^{-1}$, $-50 m \cdot s^{-1}$ and $-25 m \cdot s^{-1}$. As the pitch reduces the forward speed, the lander automatically adjusts the thruster main force in order to keep its ventral OF near the set point through the landing. With a starting vertical speed of $-50 m \cdot s^{-1}$ and $-25 m \cdot s^{-1}$ the lander reaches the low gate with acceptable ground speed and vertical speed. In the case of the large initial vertical speed (here $-100 m \cdot s^{-1}$), the autopilot can not stabilize the ventral OF and thus the lander reaches the low gate with a very high ground speed $V_{x_l} = 47.5 m \cdot s^{-1}$ and a high vertical speed $V_{h_l} = -41.5 m \cdot s^{-1}$: the lander will probably crash.

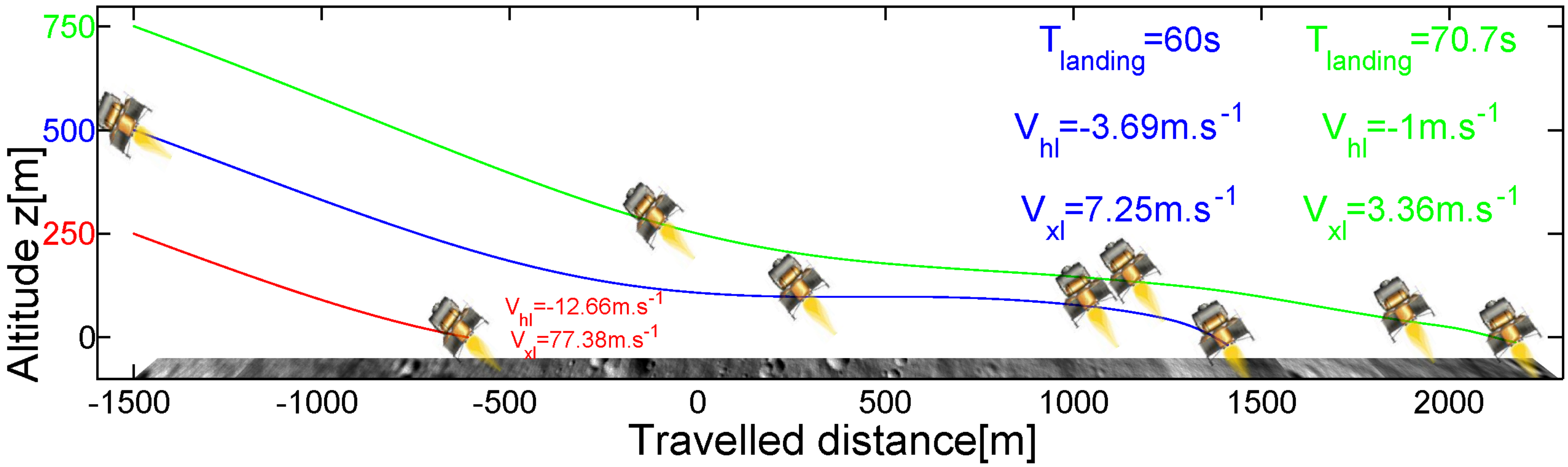

Figure 18: Automatic Landing For Different initial Altitude. We show automatic landing trajectories of a Lander for different initial altitude ($750m$ in green, $500m$ in blue and $250m$ in red), with an initial ground speed of $150m \cdot s^{-1}$ and an initial vertical speed of $-50m \cdot s^{-1}$ in regular lighting conditions. The lander is plotted every 20 seconds before it reached the low gate i.e., a ground height of $10meters$ with respect to the local ground altitude. With an initial altitude of $250m$ (red trajectory), the lander crashes, the low gate is reached in $8s$ with a ground speed of $77.4m \cdot s^{-1}$ and a vertical speed of $-12.7m \cdot s^{-1}$. With an initial altitude of $500m$ (blue trajectory), the lander reaches the low gate in $60s$ with a ground speed of $7.25m \cdot s^{-1}$ and a vertical speed of $-3.69m \cdot s^{-1}$. With an initial altitude of $750m$ (green trajectory), the lander reaches the low gate in $70.7s$ with a ground speed of $3.36m \cdot s^{-1}$ and a vertical speed of $-1m \cdot s^{-1}$.

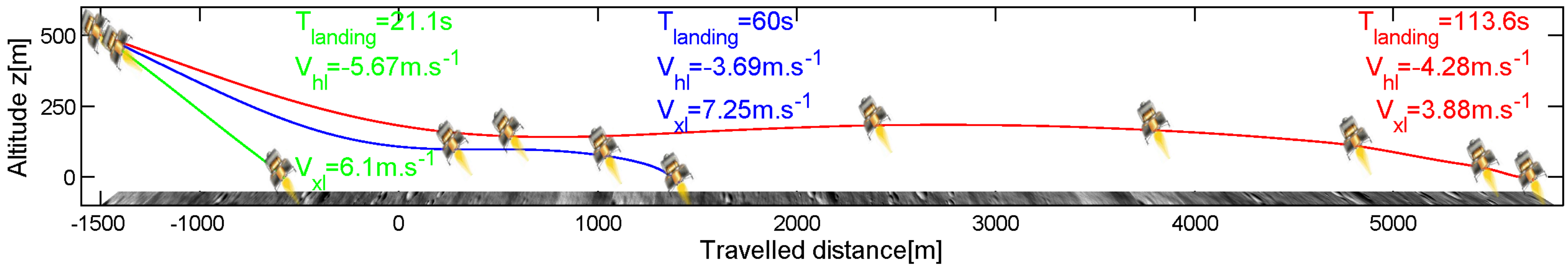

Figure 19: Automatic Landing For different initial ground speed. We show automatic landing trajectories of a lander on moon for different initial ground speed ($200m \cdot s^{-1}$ in red, $150m \cdot s^{-1}$ in blue and $100m \cdot s^{-1}$ in green), with an initial vertical speed of $-50m \cdot s^{-1}$ and an initial altitude of $500m$ in regular lighting conditions. The lander is plotted every 20 seconds before it reached the low gate i.e., a ground height of $10 meters$ with respect to the local ground altitude. With an initial ground speed of $100m \cdot s^{-1}$ (green trajectory), the lander reaches the low gate in $21s$ with a ground speed of $6.1m \cdot s^{-1}$ and a vertical speed of $-5.6m \cdot s^{-1}$. With an initial ground speed of $150m \cdot s^{-1}$ (blue trajectory), the lander reaches the low gate in $60s$ with a ground speed of $7.25m \cdot s^{-1}$ and a vertical speed of $-3.69m \cdot s^{-1}$. With an initial ground speed of $200m \cdot s^{-1}$ (red trajectory), the lander reaches the low gate in $113.6s$ with a ground speed of $3.88m \cdot s^{-1}$ and a vertical speed of $4.28m \cdot s^{-1}$.

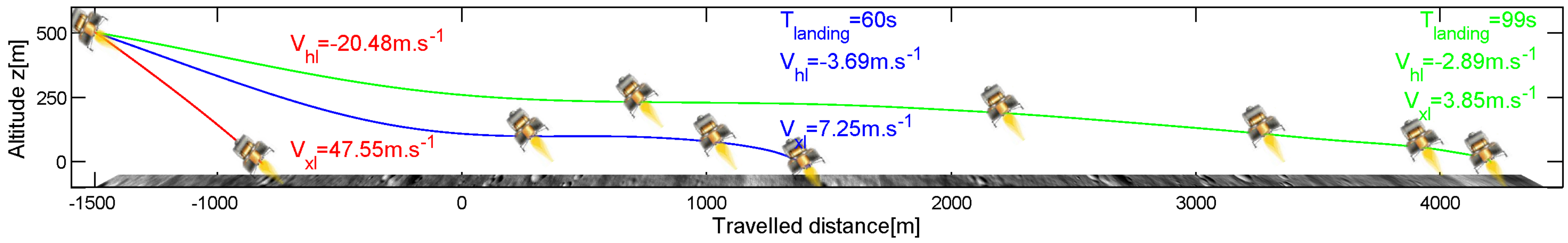

Figure 20: Automatic Landing For different initial vertical speed. We show automatic landing trajectories of the lander for different initial vertical speed ($-100m \cdot s^{-1}$ in red, $-50m \cdot s^{-1}$ in blue and $-25m \cdot s^{-1}$ in green), with an initial ground speed of $150m \cdot s^{-1}$ and an initial altitude of $500m$ in regular lighting conditions. The lander is plotted every 20 seconds before it reached the low gate i.e., a ground height of $10meters$ with respect to the local ground altitude. With an initial vertical speed of $-25m \cdot s^{-1}$ (green trajectory), the lander reaches the low gate in $99s$ with a ground speed of $3.85m \cdot s^{-1}$ and a vertical speed of $-2.89m \cdot s^{-1}$. With an initial ground speed of $-50m \cdot s^{-1}$ (blue trajectory), the lander reaches the low gate in $60s$ with a ground speed of $7.25m \cdot s^{-1}$ and a vertical speed of $-3.69m \cdot s^{-1}$. With an initial ground speed of $-100m \cdot s^{-1}$ (red trajectory), the lander crashes: the low gate is reached in $6.9s$ with a ground speed of $47.5m \cdot s^{-1}$ and a vertical speed of $-41.5m \cdot s^{-1}$.

5.4 OF measurement quality under regular and south pole lighting condition

In the figure 21 the lander reaches the low gate under regular and south pole lighting condition at low speed. In each cases, the simulated lander starts its automatic landing at an initial altitude $Z_o = 500m$, an initial ground speed $V_{x_0} = 150m \cdot s^{-1}$ and an initial vertical speed $V_{h_0} = -50m \cdot s^{-1}$. Figures 21A and 21B show the trajectory of the lander in the vertical plane (x, z) ans the position of the lander when it reaches the low gate and every 20 seconds before. The lunar surface seen by the simulated lander under regular lighting conditions is shown in figure21C and the lunar surface under south pole lighting condition is shown in figure 21D. In order to obtain the south pole lighting condition, we had to modify the following line in the "PANGU.ini" file:

```
...
sun.position      14.9e10  55  15
...
```

which is corresponding to the regular lighting condition by the following line:

```
...
sun.position      14.9e10  55  1.5
...
```

The OF measured ω^{meas} is quite the same under regular and south pole lighting condition (see figure21E and figure21F). So we can deduce that the quality of measured OF does not depend on the lighting condition. Nevertheless, the OF updating rate depends only on the occurrence rate of contrast thresholded by the OF sensor : the contrast magnitude can depend on lighting conditions even for the same terrain.

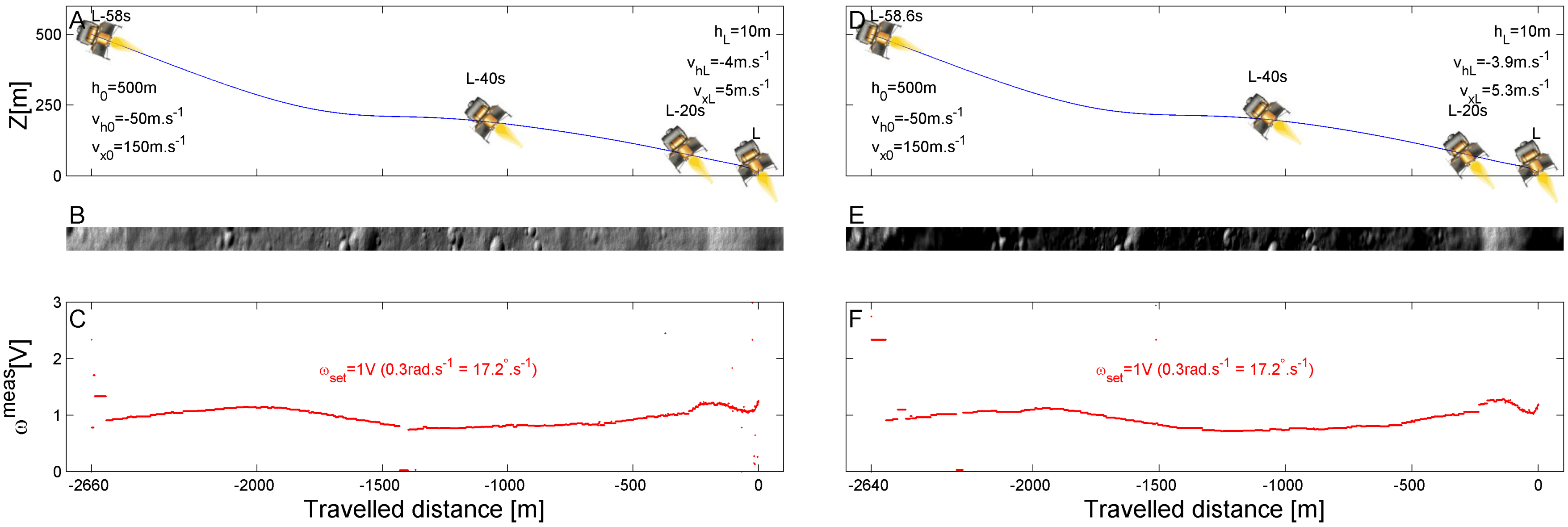

Figure 21: Comparison between automatic landing under regular and south-pole lighting conditions. (A) Lander trajectory under regular lighting condition and with an initial ground speed $V_{x0} = 150m\cdot s^{-1}$, an initial vertical speed $V_{h0} = -50m\cdot s^{-1}$ and an initial altitude $Z_0 = 500m$ (Trajectory showed in figure 13) (B) PANGU generated Moon surface under regular lighting condition as provided to the simulated lander during the the above mentioned experiments. (C) Output ω^{meas} of the OF sensor monitored during the landing under regular lighting conditions. The OF is relatively constant throughout, $\omega_{set} = 1V(0.3rad\cdot s^{-1} = 17.2^\circ \cdot s^{-1})$. (D) Landing trajectory using the identical initial settings but under lighting conditions resembling lunar south pole, i.e. sun elevation at 1.5°. (E) PANGU generated Moon surface with sun elevation at 1.5°. To compare with the previous experiments, the terrain has remained unchanged to the one presented in figure 21C. (F) Output ω^{meas} of the OF sensor as monitored when facing challenging lighting conditions. The OF also remains relatively constant throughout, $\omega_{set} = 1V(0.3rad\cdot s^{-1} = 17.2^\circ \cdot s^{-1})$.

5.5 Effect of various initial conditions with south pole lighting condition

5.5.1 Different initial height

The figure 22 shows the influence of various initial altitude under south pole lighting conditions on the landing with an initial ground speed $V_{x0} = 150m \cdot s^{-1}$and an initial vertical speed $V_{h0} = -50m \cdot s^{-1}$. The figure shows the lander trajectory in the vertical plane (x,z) and the lander when it reaches the low gate and every 20 seconds before, for a starting altitude of $750m$, $500m$ and $250m$. As the pitch reduces the forward speed, the lander automatically adjusts the thruster main force in order to keep its ventral OF near the set point through the landing. With a starting altitude of $500m$ and $750m$ the lander reaches successfully the low gate with an acceptable ground speed and vertical speed. Starting with a low altitude (here $250m$), the ventral OF increase too fast and the autopilot can not stabilize the ventral OF and thus the lander reaches the low gate with a high ground speed $V_{x_l} = 76m \cdot s^{-1}$ and a high vertical speed $V_{h_l} = -12.1m \cdot s^{-1}$: the lander will probably crash.

5.5.2 Different initial ground speed

The figure 23 shows the influence of various initial ground speed under south pole lighting conditions on the landing with an initial altitude $Z_0 = 500m$ and an initial vertical speed $V_{h0} = -50m \cdot s^{-1}$. The figure shows the lander trajectory in the vertical plane (x,z) and the lander when it reaches the low gate and every 20 seconds before, for an initial ground speed of $200m \cdot s^{-1}$, $150m \cdot s^{-1}$ and $100m \cdot s^{-1}$. As the pitch reduces the forward speed, the lander automatically adjusts the thruster main force in order to keep its ventral OF near the set point through the landing. The lander reaches successfully the low gate with an acceptable ground speed and vertical speed for every initial ground speed (i.e. $200m{\cdot}s^{-1}$, $150m{\cdot}s^{-1}$ and $100m{\cdot}s^{-1}$). Larger is the initial ground speed, farther is the distance traveled by the Lander before reaching the low gate (thus, increasing the time taken by the Lander to land on Moon).

5.5.3 Different initial vertical speed

The figure 24 shows the influence of various initial vertical speed under south pole lighting conditions on the landing with an initial altitude $Z_0 = 500m$ and an initial ground speed $V_{x0} = 150m \cdot s^{-1}$. The figure shows the lander trajectory in the vertical plane (x,z) and the lander when it reaches the low gate and every 20 seconds before, for an initial vertical speed of $-100m \cdot s^{-1}$, $-50m \cdot s^{-1}$ and $-25m \cdot s^{-1}$. As the pitch reduces the forward speed, the lander automatically adjusts the thruster main force in order to keep its ventral OF near the set point through the landing. In the case of a starting vertical speed of $-50m \cdot s^{-1}$ and $-25m \cdot s^{-1}$, the lander reaches the low gate with acceptable ground speed and vertical speed. Starting with a high vertical speed (here $-100m \cdot s^{-1}$), the autopilot can not stabilize the ventral OF and thus the lander reach the low gate with a high ground speed $V_{x_l} = 46m \cdot s^{-1}$ and a high vertical speed $V_{h_l} = -40.5m \cdot s^{-1}$: the lander will probably crash.

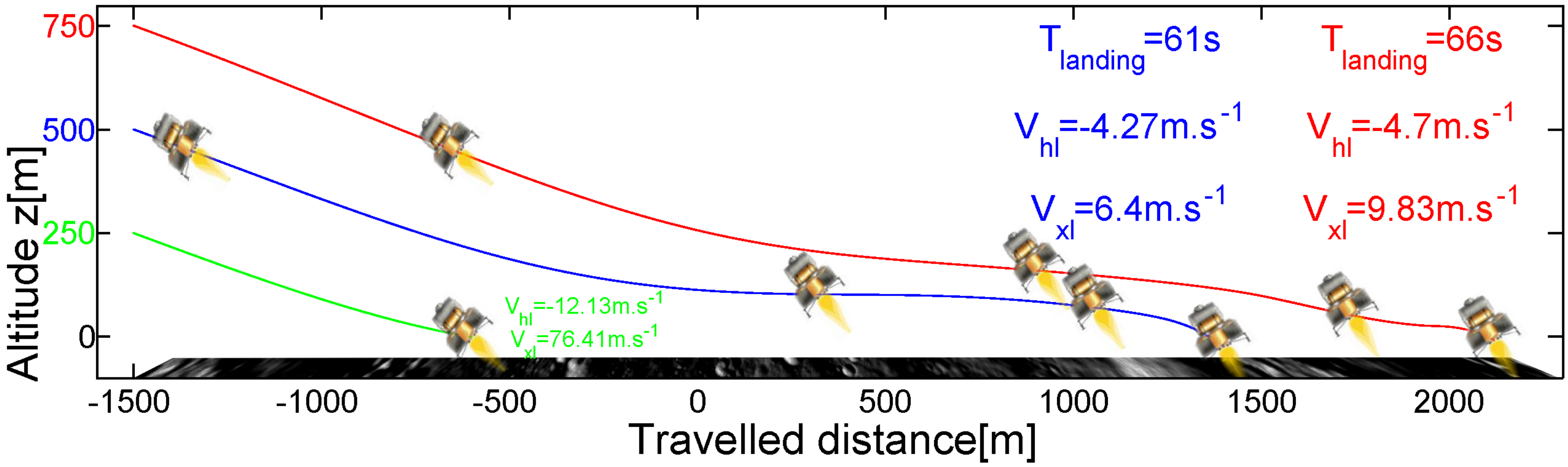

Figure 22: Automatic landing for different initial Altitude under South pole lighting conditions. We show automatic landing trajectories of a Lander for different initial altitude ($750m$ in red, $500m$ in blue and $250m$ in green), with an initial ground speed of $150m \cdot s^{-1}$ and an initial vertical speed of $-50m \cdot s^{-1}$ in South pole lighting conditions. The lander is plotted every $20seconds$ before it reached the low gate i.e., a ground height of $10meters$ with respect to the local ground altitude. With an initial altitude of $250m$ (green trajectory), the lander crashes, the low gate is reached in $8s$ with a ground speed of $76m \cdot s^{-1}$ and a vertical speed of $-12.1m \cdot s^{-1}$. With an initial altitude of $500m$ (blue trajectory), the lander reaches the low gate in $61s$ with a ground speed of $6.4m \cdot s^{-1}$ and a vertical speed of $-4.27m \cdot s^{-1}$. With an initial altitude of $750m$ (red trajectory), the lander reaches the low gate in $66s$ with a ground speed of $9.83m \cdot s^{-1}$ and a vertical speed of $-4.7m \cdot s^{-1}$.

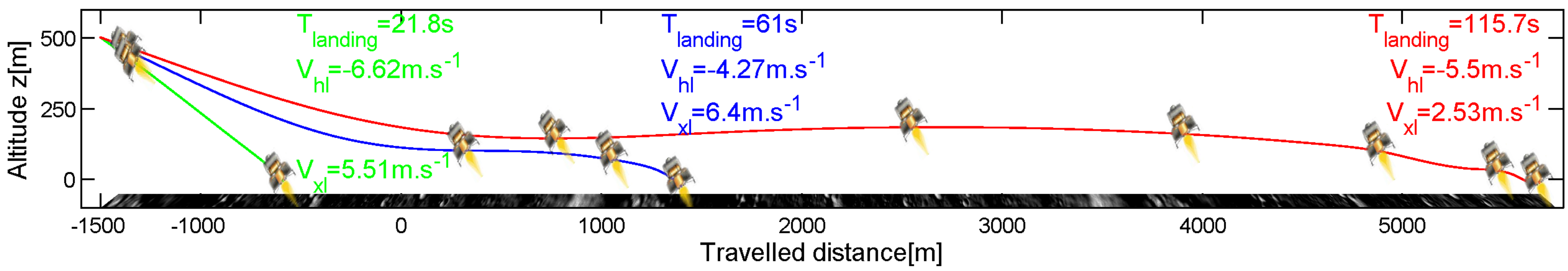

Figure 23: Automatic Landing For different initial ground speed under South pole lighting conditions. We show automatic landing trajectories of a Lander on Moon for different initial ground speed ($200m \cdot s^{-1}$ in red, $150m \cdot s^{-1}$ in blue and $100m \cdot s^{-1}$ in green), with an initial vertical speed of $-50m \cdot s^{-1}$ and an initial altitude of $500m$ in South pole lighting conditions. The lander is plotted every $20seconds$ before it reached the low gate i.e., a ground height of $10meters$ with respect to the local ground altitude. With an initial ground speed of $100m \cdot s^{-1}$ (green trajectory), the lander reaches the low gate in $21.8s$ with a ground speed of $5.51m \cdot s^{-1}$ and a vertical speed of $-6.62m \cdot s^{-1}$. With an initial ground speed of $150m \cdot s^{-1}$ (blue trajectory), the lander reaches the low gate in $61s$ with a ground speed of $6.4m \cdot s^{-1}$ and a vertical speed of $-4.27m \cdot s^{-1}$. With an initial ground speed of $200m \cdot s^{-1}$ (red trajectory), the lander reaches the low gate in $115.7s$ with a ground speed of $2.53m \cdot s^{-1}$ and a vertical speed of $-5.5m \cdot s^{-1}$.

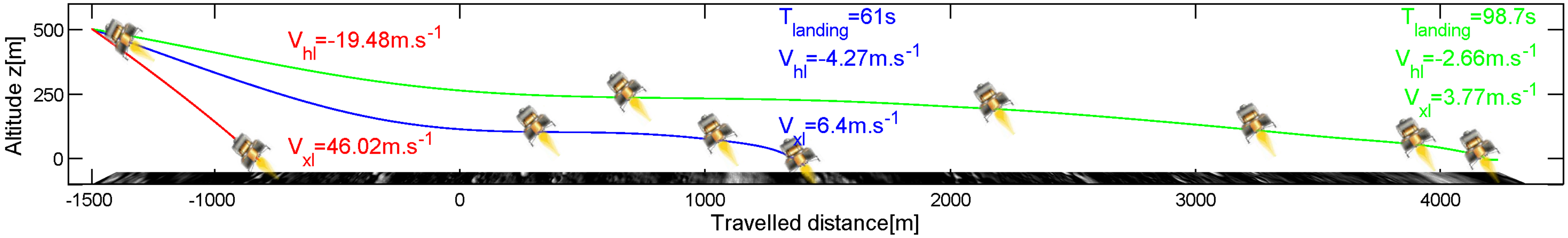

Figure 24: Automatic Landing For different initial vertical speed with South pole lightning conditions We show automatic landing trajectories of the lander for different initial vertical speed ($-100m \cdot s^{-1}$ in red, $-50m \cdot s^{-1}$ in blue and $-25m \cdot s^{-1}$ in green), with an initial ground speed of $150m \cdot s^{-1}$ and an initial altitude of $500m$ in normal lighting conditions. The lander is plotted every $20 seconds$ before it reached the low gate i.e., a ground height of $10 meters$ with respect to the local ground altitude. With an initial vertical speed of $-25m \cdot s^{-1}$ (green trajectory), the lander reaches the low gate in $98.7s$ with a ground speed of $3.77m \cdot s^{-1}$ and a vertical speed of $-2.66m \cdot s^{-1}$. With an initial ground speed of $-50m \cdot s^{-1}$ (blue trajectory), the lander reaches the low gate in $61s$ with a ground speed of $6.4m \cdot s^{-1}$ and a vertical speed of $-4.27m \cdot s^{-1}$. With an initial ground speed of $-100m \cdot s^{-1}$ (red trajectory), the lander crashes: the low gate is reached in $7s$ with a ground speed of $46m \cdot s^{-1}$ and a vertical speed of $-40.5m \cdot s^{-1}$.

5.6 Effect of a failure in the OF measurement

The figure25 shows an automatic landing with an OF sensor failure during the landing. This sensor failure represents a “no contrast” zone on the lunar surface or a real failure of the OF sensor during a few seconds. The figure 25A shows the trajectory of the lander in the vertical plane (x,z) for different OF sensor failure duration (no failure in blue, $3s$ in black, $6s$ in green and $9s$ in red) with an initial ground speed $V_{x0} = 150m \cdot s^{-1}$, an initial vertical speed $V_{z0} = -50m \cdot s^{-1}$ and an initial altitude $Z_0 = 500m$ under regular lighting conditions. The lander reaches successfully the low gate despite an OF sensor failure duration of $3s$ and $6s$ but for a failure duration of $9s$ its ground speed $V_{x_l} = 36.2m \cdot s^{-1}$ and vertical speed $V_{z_l} = -10.9m \cdot s^{-1}$ are too high and the lander will crash. The figure 25B shows that the autopilot restores the OF measured ω^{meas} to the set point value after the failure, the OF measured is approximately the same in the end of the landing phase for OF sensor failure duration of $3s$, $6s$ and for the landing without sensor failure. These results show that the autopilot makes the lander to reach the low gate without being dramatically disturbed by the ventral OF sensor failure for a maximum duration of $6s$.

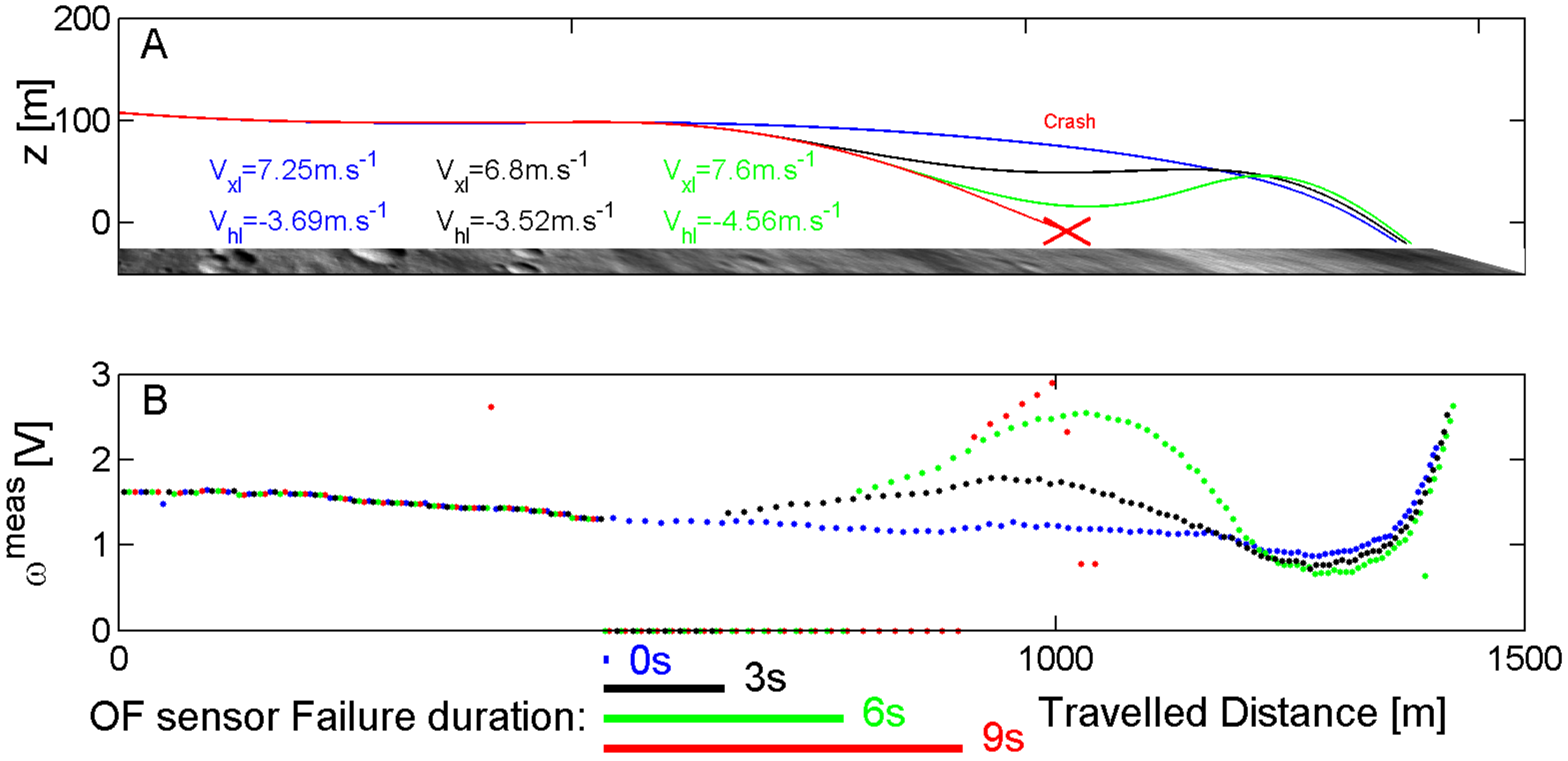

Figure 25: Effects of sensor blinding during landing. During landing with initial conditions as outlined above (see figure 13), the controller is confronted with sensor failure. Blue line: no failure, black: $3s$, green: $6s$, and red: $9s$ without OF readings respectively. (A) Lander trajectory and the lunar surface generated by PANGU. In the failure-free control situation, the lander reaches low gate in $60s$ with a vertical speed of $-3.69m \cdot s^{-1}$ and a ground speed of $7.25 \cdot s^{-1}$. When the OF sensor is blinded for $3s$ i.e., the reading values are zero (black line), the lander reaches low gate in $60.4s$ and a vertical speed of $-3.52m \cdot s^{-1}$ and a ground speed of $6.8m \cdot s^{-1}$. If the sensor blinding lasts $6s$ (green line), the lander reaches low gate in $60.3s$ with a vertical speed of $-4.56m \cdot s^{-1}$ and a ground speed of $7.6m \cdot s^{-1}$. However, if the sensor reading zero extends to $9s$ (red line), the lander crashes after $37.6s$ with a vertical speed of $-10.9m \cdot s^{-1}$ and an ground speed of $36.2m \cdot s^{-1}$. (B) Output ω^{meas} monitored during the landing at the different experimental conditions. When the sensor is functional again, the controller tries to re-establish the OF at the set point, successfully after $3s$ and $6s$ of blinding, but not after $9s$ without signal. (Note: Starting point of plant during simulation lies outside displayed data.)

6 Comparison between Moon and Mars landing conditions

The moon and the mars problem are very different :

- There is no friction on Moon due to an absence of atmosphere,

- There is some frictions on Mars due to its atmosphere. This atmosphere helps at reducing the Lander speeds and therefore helps our autopilot to make the Lander landing. These frictions are modifying the equation of the lander's motion with which we deal on moon (See equation 4).

The equations on Mars can be written as follows:

$$\begin{cases} L - \zeta_z \cdot V_z - m_{lander} \cdot g_{mars} = m_{lander} \cdot a_{lander_z} \\ \\ T - \zeta_x \cdot V_x = m_{lander} \cdot a_{lander_x} \end{cases} \tag{23}$$

where g_{mars} is the moon gravity constant, $g_{mars} = 3.7 m \cdot s^{-2}$, ζ_z and ζ_x are the translational viscous friction coefficients along X and Z-axis and $m_{lander} = 1 \cdot 10^3 kg$, the mass of the lander. The transfer function for heave and surge dynamics $G_z(s)$ and $G_x(s)$ can be written as follows:

$$\begin{cases} G_z(s) = \frac{z(s)}{F(s)} = \frac{1}{s \cdot (s + \frac{\zeta_z}{m_{lander}})} \cdot \left[\left(\frac{1/\tau_{thruster}}{1/\tau_{thruster} + s} \cdot \cos\theta_{pitch} \right) - g_{mars} \right] \\ \\ G_x(s) = \frac{x(s)}{F(s)} = \frac{1}{s \cdot (s + \frac{\zeta_x}{m_{lander}})} \cdot \left(\frac{1/\tau_{thruster}}{1/\tau_{thruster} + s} \cdot \sin\theta_{pitch} \right) \end{cases} \tag{24}$$

These equation of motion on Mars shows that there is a single integral term instead of a double integral term in the equation on the moon. Such Lander on Mars may be easier to stabilize than on moon because of the friction which help the lander to reduce both the vertical speed and the ground speed. Landing on Mars using our strategy should require a much simpler control scheme thanks to the friction of the atmosphere: the non-linear observer may be not necessary.

7 Wind gust discussion on Mars

We think that in case of an spontaneous forward or backward acceleration (i.e. due to a thruster problem), the Lander will safely land. But the lander will land on a different site in comparison to the site where the Lander will land without any spontaneous acceleration. That's why we suggest to add a second feedback loop to show that landing on a precise spot is possible. This second feedback loop will use another cue/sensor that will give the angular position of the landing site (as viewed from the Lander). Such second feedback loop will try to reject any spontaneous forward or backward acceleration (i.e. due to a thruster problem) to land precisely on the desired landing spot [16].

8 Wide Field Integration to estimate the Lander pitch

In this report, we assumed that the lander stabilizes its gaze by compensating any plant rotation, but it is not completely right. So, the OF measured is composed of a translation OF and rotational OF (see equation 25). We have to subtract the rotational term of the OF measured ω^{meas} in order to have only translation OF. To do so, we have to assess the pitch rate $\dot{\theta}_{pitch}$ with a rate gyro or to estimate the pitch by using the WFI (Wide Field Integration [13]) method. With multiple OF sensors, we can also have an estimation of the pitch angle θ_{pitch}.

$$\omega^{meas} = \omega_T + \dot{\theta}_{pitch} \tag{25}$$

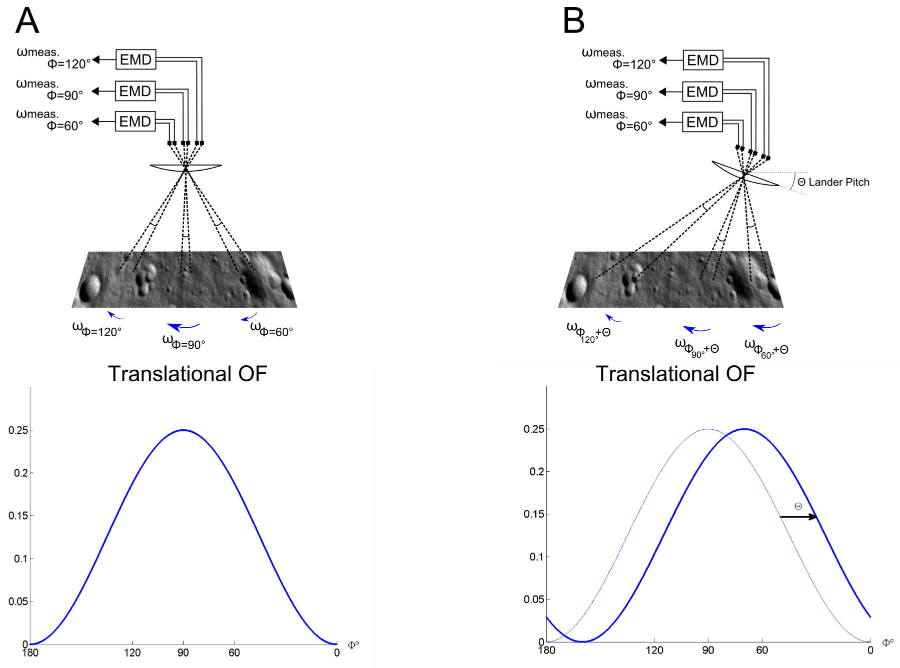

Figure 26: Generated and measured Optic flow with different pitch angle θ_{pitch}.(A) The ventral OF perceived by the Lander with a pitch angle $\theta_{pitch} = 0$ for three different orientations of OF sensor ($\Phi = 60°$, $\Phi = 90°$ and $\Phi = 120°$). The OF measured is maximum for the OF sensor orientation of 90° with respect of the lander. (B) The ventral OF perceived by the Lander with a pitch angle $\theta_{pitch} = \Theta$ for three OF sensor different orientation ($\Phi = 60°$, $\Phi = 90°$ and $\Phi = 120°$). We show that the maximum of the OF measured is not for a sensor orientation of 90°, there is a shift of the curve equal to the pitch angle $\theta_{pitch} = \Theta$. With such a sensor disposition, we can estimate the pitch of the lander.

8.1 Pitch estimation under pure translational OF

With multiple OF sensor oriented with different angle Φ, we can try to estimate the pitch θ_{pitch} of the lander. A pure translational optic flow can be written as follow:

$$\omega_T = \frac{V_x}{h} \cdot \sin^2(\Phi + \theta_{pitch}) \tag{26}$$

where Φ is the orientation angle of the OF sensor considered, and θ_{pitch} the pitch angle of the lander.

With this kind of OF sensor disposition and the new expression (see equation 26) for the translational OF, we can estimate the pitch θ_{pitch}. The equation 26 can be developed $\forall \Phi \in [0; \pi]$ as follows:

$$\omega_T = \frac{Vx}{h} \cdot (\sin\Phi \cdot \cos\theta_{pitch} - \cos\Phi \cdot \sin\theta_{pitch})^2 \tag{27}$$

and for an angle $\Phi = 90°$:

$$\omega_T^{\Phi=90°} = \frac{Vx}{h} \cdot \cos^2(\theta_{pitch}) \tag{28}$$

Using the equations 27 and 28, we can estimate the pitch angle θ_{pitch} with only three OF sensor, one with an orientation $\Phi_1 = 90°$ and the two other with an orientation Φ_2 and $\Phi_3 = \pi - \Phi_2$, $\Phi_2, \Phi_3 \in [0; \pi]$(e.g. $\Phi_2 = 60°$ and $\Phi_3 = 120°$ in the figure 26). Using the fact that $\Phi_3 = \pi - \Phi_2$, and thus $\sin\Phi_3 = \sin\Phi_2$ and $\cos\Phi_3 = -\cos\Phi_2$, we can write :

$$\frac{\omega_T^{\Phi_3} - \omega_T^{\Phi_2}}{\omega_T^{\Phi=90°}} = \frac{4 \cdot \sin\Phi_2 \cdot \cos\Phi_2 \cdot \sin\theta_{pitch} \cdot \cos\theta_{pitch}}{\cos^2\theta_{pitch}} \tag{29}$$

We can deduce from 29 the expression of the pitch angle θ_{pitch}:

$$\theta_{pitch} = \arctan\left(\frac{\omega_T^{\Phi_3} - \omega_T^{\Phi_2}}{4 \cdot \sin\Phi_2 \cdot \cos\Phi_2 \cdot \omega_T^{\Phi=90°}}\right) \tag{30}$$

8.2 Pitch rate estimation using WFI method

But, when the lander pitch forward or backward, there is a rotational Optic Flow component in the OF measured due to the pitch rate of the lander $\dot{\theta}_{pitch}$. So, we need to estimate the lander pitch rate and subtract it to the OF measured. The Wide Field Integration method [13] can allow us to estimate the pitch rate of the lander using multiple OF sensors. Considering the measured OF (sum of the rotation OF and the translational OF), the OF sensor output can be written as an inner product of the OF ω_{meas} and a pondering function F_i:

$$z_i(x) = <\omega_{meas_i}, F_i> = \frac{1}{\pi} \int_0^{2\pi} \omega^{meas}(\Phi, x) \cdot F_i(\Phi) d\Phi \tag{31}$$

We can project onto trigonometric Fourier Series and the expression becomes:

$$\omega^{meas}(\Phi, x) = \frac{a_0(x)}{2} + \sum_{n=1}^{\infty} a_n(x) \cdot \cos n\Phi + \sum_{n=1}^{\infty} b_n(x) \cdot \sin n\Phi \tag{32}$$

The expression of the Fourier coefficients can be written as follows:

$$\begin{cases} a_0(x) = \frac{1}{\pi} \cdot \int_0^{2\pi} \omega^{meas}(\Phi, x)/\sqrt{2} \cdot d\Phi \\ a_n(x) = \frac{1}{\pi} \cdot \int_0^{2\pi} \omega^{meas}(\Phi, x) \cdot \cos(n\Phi) \cdot d\Phi \\ b_n(x) = \frac{1}{\pi} \cdot \int_0^{2\pi} \omega^{meas}(\Phi, x) \cdot \sin(n\Phi) \cdot d\Phi \end{cases} \tag{33}$$

These expression can be written in discretized form as follows:

$$\begin{cases} a_0(x) = \sum_{i=1}^{k} \omega^{meas}(\Phi_i, x)/\sqrt{2} \\ a_n(x) = \sum_{i=1}^{k} \omega^{meas}(\Phi_i, x) \cdot \cos(n\Phi_i) \\ b_n(x) = \sum_{i=1}^{k} \omega^{meas}(\Phi_i, x) \cdot \sin(n\Phi_i) \end{cases} \tag{34}$$

where k is the number of OF sensor on board. The WFI method allows us to compute the pitch rate of the lander using the linearized coefficients of the Fourier transform for a planar surface geometry (table 1, column 3 in [13]):

$$a_0 = -\sqrt{2} \cdot \dot{\theta}_{pitch} - \frac{1}{2\sqrt{2} \cdot h} V_x \tag{35}$$

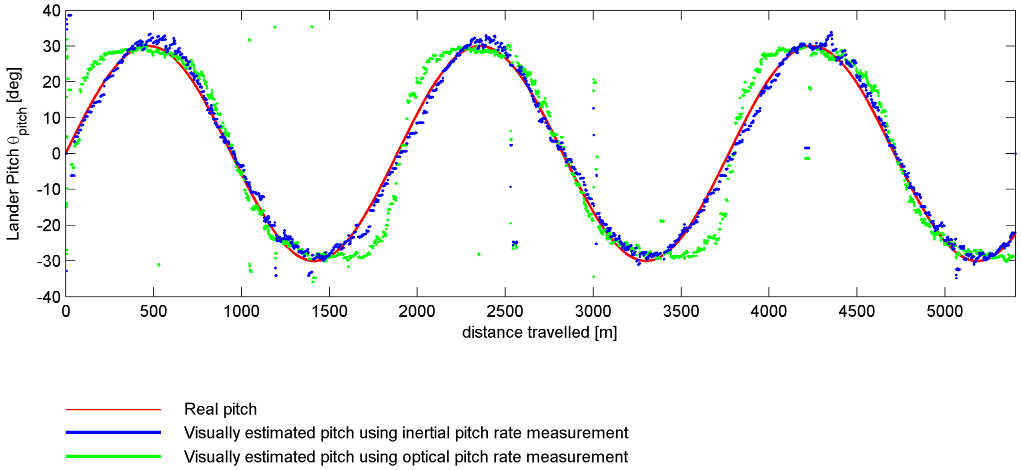

Figure 27: Pitch angle estimated using three OF sensors (see equation 38). The lander traveled at a constant altitude $z = 150m$, a constant ground speed Vx=90m/s and a vertical speed equals to zero. We applied sinusoidal variation of the pitch angle between 30° and -30°. The OF is measured by five EMD in order to have enough measurement to estimate the pitch angle of the lander. Each EMD has a different orientation angle Φ (Fig26) $(60, 75, 90, 105 and 120^{\circ})$. The OF measured by each sensor contain a translational and a rotational term, to estimate the pitch we need only the Translational Optic Flow, so we subtract the rotational term by two different methods: inertial pitch rate measurement and optical pitch rate measurement [13]. The blue plot shows the visually estimated pitch using the inertial pitch rate measurement. The green plot shows the visually estimated pitch using the optical pitch rate measurement. The visual estimation using the inertial pitch rate measurement is quite good compared to the real pitch (red plot), but there is some errors for the visual estimation using the optical pitch rate measurement. These errors are due to the number of sensors we used, this method require at least four sensors to compute the necessary Fourier coefficients, but the larger the number of sensors, the better the pitch rate estimation is.

$$a_2 = \frac{1}{4h} \cdot V_x$$

we compute $\dot{\theta}_{pitch}$by combining a_0 and a_2:

$$\dot{\theta}_{pitch} = f\left(a_0, a_2\right) = -\left(\frac{\sqrt{2}}{2} \cdot a_0 + a_2\right) \tag{36}$$

8.3 Lander's Pitch estimation with WFI method

Using 25, 36 and 30, we established that the pitch angle θ_{pitch} can be written as follows in the case of OF composed of Translational OF and rotational OF:

$$\omega_T = \omega^{meas} - \omega_R \tag{37}$$

with $\omega_R = \dot{\theta}_{pitch}$, so, we can write:

$$\theta_{pitch} = \arctan\left(\frac{\left(\omega_{\Phi_3}^{meas} - \dot{\theta}_{pitch}\right) - \left(\omega_{\Phi_2}^{meas} - \dot{\theta}_{pitch}\right)}{4 \cdot \sin\Phi_2 \cdot \cos\Phi_2 \cdot \left(\omega_{\Phi=90}^{meas} - \dot{\theta}_{pitch}\right)}\right) \tag{38}$$

Only three OF sensors measurement are necessary to estimate the pitch angle θ_{pitch}, but we need at least five OF sensors to compute the pitch rate, and thus because we have to compute a 2nd order Fourier coefficient. With respect of Shannon-Nyquist theorem, the number of sensors must be upper or equal to twice the order of the coefficient we want to compute.

Using PANGU software, we have simulated a lander with five OF sensors with different orientation angle Φ ($\Phi_1 = 90^{\circ}$, $\Phi_2 = 60^{\circ}$, $\Phi_3 = 120^{\circ}$,$\Phi_4 = 75^{\circ}$ and $\Phi_5 = 105^{\circ}$) and with a pitch

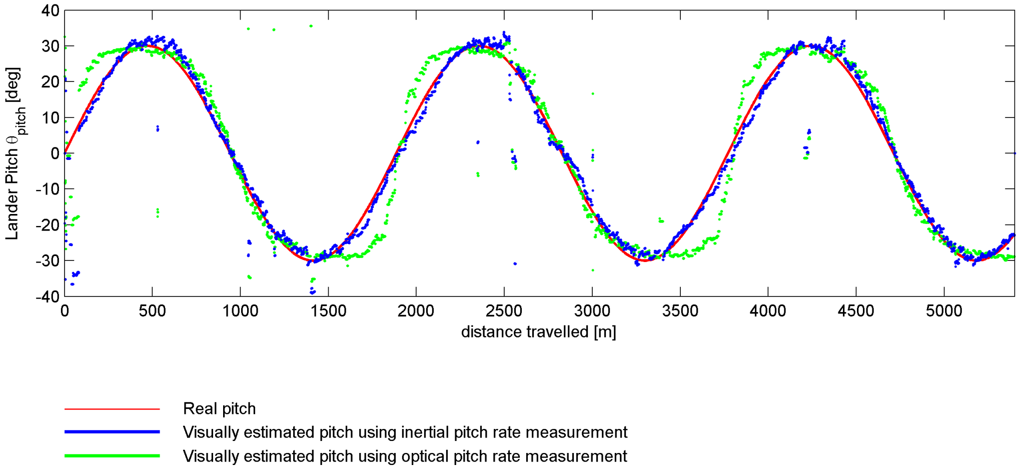

Figure 28: Pitch angle estimated using five OF sensors (see equation 39). The lander traveled at a constant altitude $z = 150m$, a constant ground speed Vx=90m/s and a vertical speed equals to zero. We applied sinusoidal variation of the pitch angle between 30° and $-30°$. The OF is measured by five EMD in order to have enough measurement to estimate the pitch angle of the lander. Each EMD has a different orientation angle Φ (see figure26) $(60, 75, 90, 105 and 120°)$. The OF measured by each sensor contain a translational and a rotational term, to estimate the pitch we need only the Translational Optic Flow, so we subtract the rotational term by two different methods: inertial pitch rate measurement and optical pitch rate measurement [13]. The blue plot shows the visually estimated pitch using the inertial pitch rate measurement. The green plot shows the visually estimated pitch using the optical pitch rate measurement. The visual estimation using the inertial pitch rate measurement is quite good compared to the real pitch (red plot), but there is some errors for the visual estimation using the optical pitch rate measurement. These errors are due to the number of sensors we used, this method require at least four sensors to compute the necessary Fourier coefficients, but the larger the number of sensors, the better the pitch rate estimation is.

angle θ_{pitch} varying sinusoidally from 30° to $-30°$ at $F_{pitch} = 47.7e^{-3}Hz$, where $F_{pitch}$is the frequency of the pitch oscillation. The result shows in figure27 show that we can have a well estimation of the lander pitch angle θ_{pitch} without any inertial measurement, only with optical measurement and with only an inertial pitch rate measurement.

We can also estimate the pitch angle θ_{pitch}using the five OF sensors used for the WFI method, the pitch angle θ_{pitch}can be written as follows:

$$\theta_{pitch} = \arctan\left(\frac{1}{2}\cdot\left(\frac{\left(\omega_{\Phi_3}-\dot{\theta}_{pitch}\right)-\left(\omega_{\Phi_2}-\dot{\theta}_{pitch}\right)}{4\cdot\sin\Phi_2\cdot\cos\Phi_2\cdot\left(\omega_{\Phi=90}-\dot{\theta}_{pitch}\right)}+\frac{\left(\omega_{\Phi_5}-\dot{\theta}_{pitch}\right)-\left(\omega_{\Phi_4}-\dot{\theta}_{pitch}\right)}{4\cdot\sin\Phi_4\cdot\cos\Phi_4\cdot\left(\omega_{\Phi=90}-\dot{\theta}_{pitch}\right)}\right)\right) \tag{39}$$

The results are showed in the figure 28, the results are quite similar but the standard deviation seems to be better when we are using five OF sensors to estimate the pitch angle θ_{pitch}.

9 Conclusion

We have presented an OF-based autopilot. Results show that a lander equipped with this autopilot can land safely under visual control. A safe landing occurs even if the lighting condition are dark (e.g. south pole lighting conditions), with various initial condition and even if the OF sensor have a few seconds failure. These feats are all achieved with a really minimalistic visual system, which consists of only two pixels i.e., two photo-receptors, forming one EMD. Key to the working of the autopilot is the OF regulator that aim at maintaining the perceived OF constant by acting upon the Thruster main forces. This OF regulator operates as follows:

The OF regulator adjusts the lander thrust so as to keep the ventral OF measured ω_{meas} equals to the OF set point ω_{set}. The outcome is that the lander's ground speed and vertical speed decrease all along the landing phase due to the coupling between the heave and surge dynamics and the lander reach the low gate at low speed.

The great advantage of this visuomotor control system is that it operates without any needs for explicit knowledge of speed and distance, and hence without any needs for speed and range sensors. The simulated lander navigates on the basis of one parameter only: the ventral OF.

References

[1] E Baird, M V Srinivasan, S Zhang, and A Cowling. Visual control of flight speed in honeybees. *J. Exp. Biol.*, 208:3895–3905, 2005.

[2] E Baird, M V Srinivasan, S Zhang, R Lamont, and A Cowling. Visual control of flight speed and height in honeybee. *LNAI*, 4095:40–51, 2006.

[3] C. Blanes. *Appareil visuel elementaire pour la navigation a vue d'un robot mobile autonome.* Master thesis in Neurosciences (DEA in French), Neurosciences, Univ. Aix-Marseille II, Marseille, 1986.

[4] C Blanes. *Guidage visuel d'un robot mobile autonome d'inspiration biologique 2nde Partie.* PhD thesis, Thèse de doctorat, Grenoble: Institut National Polytechnique de Grenoble (INP Grenoble), 1991.

[5] P de Larminat. *Automatique applique.* Hermes sciences, 2007.

[6] N Franceschini. Early processing of color and motion in a mosaic visual system. *Neurosc. Res. Suppl.*, 2:517–549, 1985.

[7] N. Franceschini, C. Blanes, and L. Oufar. *'Passive, non- contact optical velocity sensor' (in French.* Dossier technique ANVAR/DVAR N 51 549, Paris, 1986.

[8] N. Franceschini, A. Riehle, and A. Le Nestour. *Directionally Selective Motion Detection by Insect Neurons*, pages 360–390. D.G. Stavenga, R.C. Hardie, Eds., Springer, Berlin, 1989.

[9] N. Franceschini, F. Ruffier, and J. Serres. A bio-inspired flying robot sheds light on insect piloting abilities. *Current Biology*, 17(4):329–335, 2007.

[10] N Franceschini, F Ruffier, J Serres, and S Viollet. *Aerial vehicles*, chapter Optic flow based visual guidance: from flying insects to miniature aerial vehicles, pages 747–770. In-Tech, 2009.

[11] J.J. Gibson. *The perception of the visual world.* Houghton Mifflin, Boston, 1950.

[12] G A Horridge. The evolution of visual processing of seeing system. *Proc. Roy. Soc. Lond. B*, 230:279–292, 1987.

[13] J.S. Humbert and M.A. Frye. Extracting behaviorally relevant retinal image motion cues via wide-field integration. In *Proc. of the American Control Conference*, Minneapolis, MN, USA, 2006.

[14] S M Parkes, I Martin, M Dunstan, and D Matthews. Planet surface simulation with pangu. In *8th International Conference on Space Operations (SpaceOps 2004), Montreal, Canada, May 17-21*, 2004.

[15] R Preiss. Motion parralax and figural properties of depth control flight speed in an insect. *Biol. Cyb.*, 57:1–9, 1987.

[16] F Ruffier and N Franceschini. Steering aid method and system for landing on a target of a moving platform, and a 3d vehicle equipped as such. patent number: Ep082900961.5. Technical report, CNRS, universit de la mediterrane, Marseille, 13/10/2008.

[17] F. Ruffier and N. Franceschini. Visually guided micro-aerial vehicle : automatic take off, terrain following, landing and wind reaction. In *Proceeding of IEEE International Conference on Robotics and Automation (ICRA 2004)*, pages 2339–2346, New Orleans, USA, 2004.

[18] F. Ruffier and N. Franceschini. Optic flow regulation: the key to aircraft automatic guidance. *Robotics and Autonomous Systems*, 50(4):177–194, 2005.

[19] F. Ruffier, S. Viollet, S. Amic, and N. Franceschini. Bio-inspired optical flow circuits for the visual guidance of micro-air vehicles. In *Proc. of IEEE Int. Symposium on Circuits and Systems (ISCAS)*, pages Vol. III, pp. 846–849, Bangkok, Thailand, 2003.

[20] J Serres, F Ruffier, J P Masson, and N Franceschini. A bee in a corridor: centering or wall following? In *Proc. of the 7th meeting of the German neuroscience society - 31st Göttingen neurobiology conference*, 2007.

[21] A W Snyder. Acuity of compond eyes: Physical limitations and design. *J. comp. physiol. A*, 116:161–182, 1977.

[22] M V Srinivasan, M Lehrer, W H Kirchner, and S Zhang. Range perception through apparent image speed in freely flying honeybees. *Vis. Neurosci.*, 6:519–535, 1991.

[23] M.V. Srinivasan, S.W. Zhang, J. Chahl, E. Barth, and S. Venkatesh. How honeybees make grazing landings on flat surfaces. *Biological Cybernetics*, 83(3):171–183, 2000.

[24] M.V. Srinivasan, S.W. Zhang, M. Lehrer, and T.S. Collett. Honeybee navigation en route to the goal: visual flight control and odometry. *J. Exp. Biol.*, 199:237–244, 1996.